Metabolic specialization drives reduced pathogenicity in *Pseudomonas aeruginosa* CF clinical isolates

Bjarke H. Pedersen [1], Filipa B. Simões [2], Ivan Pogrebnyakov [1], Martin Welch [3], Helle Krogh Johansen [2,4], Søren Molin [1] and Ruggero La Rosa [1,2#]

[1] The Novo Nordisk Foundation Center for Biosustainability, Technical University of Denmark, 2800 Kgs. Lyngby, Denmark

[2] Department of Clinical Microbiology 9301, Rigshospitalet, 2100 Copenhagen, Denmark

[3] Department of Biochemistry, University of Cambridge, CB2 1TN Cambridge, United Kingdom

[4] Department of Clinical Medicine, Faculty of Health and Medical Sciences, University of Copenhagen, 2200 Copenhagen, Denmark

Address correspondence to Ruggero La Rosa, rugros@biosustain.dtu.dk

Abstract

Metabolism provides the foundation for all cellular functions. During persistent infections, in adapted pathogenic bacteria metabolism functions radically differently compared with more naïve strains. Whether this is simply a necessary accommodation to the persistence phenotype or if metabolism plays a direct role in achieving persistence in the host is still unclear. Here, we characterize a convergent shift in metabolic function(s) linked with the persistence phenotype during *Pseudomonas aeruginosa* colonization in the airways of people with cystic fibrosis. We show that clinically-relevant mutations in the key metabolic enzyme, pyruvate dehydrogenase, lead to a host-specialized metabolism together with a lower virulence and immune response recruitment. These changes in infection phenotype are mediated by impaired type III secretion system activity and by secretion of the antioxidant metabolite, pyruvate, respectively. Our results show how metabolic adaptations directly impinge on persistence and pathogenicity in this organism.

Introduction

Difficult to treat bacterial infections are increasing around the world [1]. While antibiotic resistance is a major cause of treatment failure, other less characterized mechanisms rooted in the complexity of the host-pathogen interactions are also substantial contributors to persistence [2]. Genetic variants with high tolerance to stresses, host and immune evasion capabilities and low virulence are often specifically selected for in persistent infections since they provide higher within-host fitness [3,4]. In people with cystic fibrosis (pwCF), for example, opportunistic pathogens such as *Pseudomonas aeruginosa* colonize the airways and establish persistent infections lasting for more than 30 years. During the infection, they differentiate into heterogeneous populations specifically evolved for the host microenvironment [5–7]. Surprisingly, antibiotic resistance is not the initial driver of persistence since bacteria retain antibiotic susceptibility for years after colonization [8]. Seemingly, these populations use mechanisms of persistence such as biofilm formation, loss of flagella and virulence factors, growth rate reduction, immune escape, and metabolic specialization to hide from the immune system and withstand the antibiotic treatment [2]. These mechanisms usually fall below the detection radar since, in simple laboratory conditions, without the intrinsic

53 complexity of the host environment and its interactions with the bacteria, no assumptions on
54 the persistence of such populations can be made. However, these mechanisms are relevant
55 for the overall persistence of the infecting population, possibly being the main drivers of the
56 initial host colonization before the insurgence of antibiotic resistance.

57 One hypothesis is that metabolic specialization strongly influences the host-pathogen
58 interactions and leads to persistence [9,10]. Metabolism of bacterial pathogens is, indeed, a
59 central process involved both in cell duplication and in virulence. In many infections, the
60 nutrient composition of the host microenvironment provides an environmental cue for
61 bacterial pathogens to activate their virulence repertoire [10]. Abnormalities in calcium
62 homeostasis, nutrient limitation or change in pH can for example trigger the type III secretion
63 system (T3SS) cascade in several bacterial species, activating the secretion of virulence
64 effectors promoting colonization of the host [11–14]. In *P. aeruginosa*, the T3SS has a key role
65 during infection, since through its injectosome and secreted factors, it subverts the host cell
66 machinery influencing both invasion, growth, and host immune response [11,15,16]. Similarly,
67 metabolism-dependent processes such as biofilm production and mucoidy provide shielding
68 from antibiotics and immune cells and are generally associated with worse prognoses [17–19].
69 Furthermore, crosstalk between bacteria and immune cells through exchange of bacterial and
70 host metabolites has additionally revealed the importance of metabolism in determining the
71 outcome of an infection [20–22]. Importantly, metabolism is not a static function; it dynamically
72 changes to support cell growth and virulence specifically for each host and type of infection.
73 Clinical strains of *P. aeruginosa* that infect pwCF, have been shown to modify their metabolic
74 preference to accommodate the specific nutrient composition of the airways [23,24].
75 Auxotrophy, specialized assimilation of carbon sources, secretion of high value metabolites
76 and differential oxygen requirements of adapted clinical strains ensure appropriate
77 functionality of the cell and support the phenotype requirements in the host [9]. However, it is
78 still unclear if and how metabolic specialization directly contribute(s) to persistence [23,25].
79 Furthermore, the specific selective forces (for example antibiotic treatment or the immune
80 system) leading to metabolic specialization still remain uncharacterized. Few examples of
81 laboratory studies in *P. aeruginosa* and *Escherichia coli* have suggested the involvement of
82 specific metabolic mutations with changes in antibiotic susceptibility and virulence [26–30].
83 However, limited knowledge is available on their relevance and purpose in clinical isolates of

84 *P. aeruginosa* during an infection. Moreover, the extent to which metabolic specialization *per*
85 *se* provides a specific fitness advantage or if it is merely a downstream effect of
86 accommodating other essential phenotypes still remains unknown. For example, it has been
87 shown that overexpression of multidrug efflux pumps causing antibiotic resistance, can lead
88 to rewired metabolism to compensate for its fitness cost [31]. However, if such mechanism is
89 generalizable and if it specifically contributes to persistence is still undisclosed. Importantly,
90 previous metabolic characterizations of clinical strains were carried out only on a limited
91 number of isolates and/or on bacterial cultures at one specific growth phase (exponential or
92 stationary phase) lacking the dynamicity of metabolic processes. Because of technical
93 challenges related to the complexity of dynamic metabolomic analysis and its interpretation,
94 large scale analyses of populations of clinical isolates that account for the inherent dynamicity
95 of metabolism have so far been lacking. Moreover, the effect of metabolic specialization on
96 the host-pathogen interactions remains unclear, limiting the understanding of its contribution
97 to persistence [2,32]. It is, therefore, crucial to systematically identify and characterize new
98 mechanisms of metabolic specialization to build a comprehensive understanding of the
99 contribution of metabolism to persistence. Such efforts will provide new understanding of
100 treatment failure and unravel new pathogen vulnerabilities and therapeutic options, which
101 are currently overshadowed by the focus on increasing antibiotic resistance.

102 Here, we identify and characterize molecular mechanisms of metabolic specialization
103 occurring in clinical strains of *P. aeruginosa* during persistence in pwCF, which have an impact
104 on the relationship between the host and the pathogen and, therefore, persistence. By
105 analyzing in detail, the metabolic and proteomic profiles of clinical strains from pwCF at
106 different stages of within-host evolution, we identified distinct metabolic configurations
107 characterized by CF-specific nutrient assimilation and secretion patterns. This was caused by
108 metabolic mutation and changes in proteome allocation. Additionally, we characterized a
109 specific mechanism of metabolic specialization involving the pyruvate dehydrogenase
110 complex (PDHc), which is essential for the processive flux of pyruvate through central carbon
111 metabolism. Surprisingly, recombinant strains containing single mutations in the PDHc show
112 decreased infection capabilities and immunogenicity in an Air-Liquid Interface (ALI) infection
113 model system. These strains display a chronic infection phenotype and an increased secretion
114 of pyruvate, which is an important scavenger of reactive oxygen species (ROS) and has known

115 anti-inflammatory properties [33–35]. Importantly, these mutations are widespread in clinical
116 isolates of *P. aeruginosa* from different patients and infection scenarios. This suggests that
117 metabolic specialization might be specifically selected for during the early stages of an
118 infection by limiting host-dependent inflammation. Altogether these results provide a
119 rationale for metabolic specialization during CF airway infections.

120

121 **Results**

122 *Strain collection for metabolomic analyses*

123 To identify molecular mechanisms of metabolic specialisation which modify the interactions
124 between the host and the pathogen occurring during the infection of pwCF, we selected from
125 our longitudinal collection of 474 *P. aeruginosa* clinical strains [36] pairs of early (*_E; first *P.*
126 *aeruginosa* isolated from the person) and late (*_L) clinical isolates, longitudinally isolated
127 from eight different pwCF (Fig. 1a). To increase the odds of selecting strains presenting
128 undisclosed mechanisms of metabolic specialization, we used growth rate as a proxy for
129 within-host evolution. Previous studies have, indeed, shown that slow growth is an important
130 phenotype associated with adaptive evolution to the CF airways, appearing within the first 2-
131 3 years of the infection [8]. The genome of each isolate had been previously sequenced and
132 their genotype determined [36]. Specifically, each pair of early and late clinical isolates are
133 phylogenetically related, and belong to the same "clone type" (defined as genomes sharing
134 more than 10,000 SNPs) (Fig. 1a). Each pwCF was colonized by a distinct clone type with
135 evolutionary histories spanning between 1.4 and 7 years (Table S1). This strategy allowed us
136 to investigate metabolic adaptations in a diverse collection of 16 clinical strains belonging to
137 8 distinct clone types. When grown in Synthetic Cystic Fibrosis Medium 2 (SCFM2) (which has
138 been formulated to resemble the CF mucus composition [37]), early isolates showed a high
139 growth rate, comparable to the reference strain, PAO1. Conversely, late isolates showed a
140 2.2- to 5.1-fold reduction in growth rate, in addition to a lower maximal optical density (paired
141 t test, P = 0.002) (Fig. 1a-b). Moreover, some late isolates were unable to grow in minimal
142 medium in presence of single carbon sources such as glucose, lactate or succinate, indicative
143 of a metabolic constraint such as auxotrophy [38] (Fig. 1c).

144

145 *Within-host evolution selects for specialized metabotypes*

146 To evaluate the degree of metabolic specialization in the clinical isolates, dynamic exo-
147 metabolomics was performed on cells growing in SCFM2 (Supplementary Data 1). This
148 approach allows for analysis of the assimilation and secretion patterns of specific metabolites
149 during the growth of each isolate, providing a dynamic snapshot of their metabolic activity.
150 PCA of the extracellular metabolomes revealed the presence of three distinct specialized
151 metabolic configurations in late strains, hereafter defined as "adapted metabotypes" (DK15
152 and DK55 metabotype 1; DK12 metabotype 2; DK03, DK13 and DK36 metabotype 3). These
153 metabotypes separate the late isolates from each respective early isolate and from the rest
154 of the non-adapted metabotypes, hereafter defined as "naïve metabotypes" (Fig. 2a). Note
155 that whereas PCA emphasizes the largest differences in the metabolomic profiles, the
156 hierarchical cluster analysis (HCA) clearly separates the early strains from the late strains,
157 indicating a certain degree of metabolic specialization in all late isolates (Fig. 2b). Indeed, both
158 the hierarchy of assimilation (metabolite half-lives, OD_{50}) which represents the order of
159 assimilation of the available carbon sources, and the secretion of metabolites differ between
160 early and late isolates (Fig. 2c-d). Specifically, adapted metabotype 1 is associated with
161 reduced assimilation of Lys, Gly, Ile, Leu, Phe, Thr, Tyr and Val, and secretion of pyruvate by
162 strain DK55 late; metabotype 2 shows increased assimilation of glucose, Ala, Asp, Glu, Gly,
163 Pro, Ser, Arg and His, and secretion of a high amount of pyruvate; and metabotype 3 shows
164 increased assimilation of glucose and lactate, differential assimilation of Ala, Asp, Glu, His and
165 Pro and secretion of pyruvate by strain DK36 late (Fig. 2c-d). Late DK13, DK36 and DK41 strains
166 secrete a low amount of formate whereas all late isolates secrete acetate, albeit at different
167 concentrations and with different growth-dependent profiles (Fig. 2d). Unsurprisingly, the net
168 balance between assimilated and secreted metabolites (total mM) varies between early and
169 late strains (Fig. 2e), which positively correlates with the lower biomass of the late isolates
170 (Pearson's r = 0.9; P = 0.0023) (Fig. 1b and 2e). In other words, a high percentage of
171 assimilated carbon sources are catabolized in the late isolates and secreted back into the
172 culture medium, thus limiting their availability for biomass production. This suggests either a
173 specific metabolic configuration for the late isolates - the objective of which is not biomass
174 accumulation - or an apparent inefficient metabolism.

175

176 *Changes in proteome allocation supports the metabolic specialization of clinical isolates*

177 To test the hypothesis that the observed metabolic specialization is partially rooted in
178 changes in expression of proteins involved in cellular metabolism, we analysed the proteome
179 of each clinical strains. To this end, we performed whole cell proteomics to compare protein
180 expression profiles between PAO1, early, and late strains (comparisons being early *vs* PAO1,
181 late *vs* PAO1 and late *vs* early). This allowed us to evaluate proteome changes in the clinical
182 isolates relative to a laboratory reference strain (early *vs* PAO1, late *vs* PAO1) and to identify
183 in the clinical isolates possible molecular mechanism(s) underpinning the metabolic
184 specialization we observed (late *vs* early). Of the 2061 proteins identified, 740 were
185 differentially expressed in at least one comparison (early *vs* PAO1 or late *vs* early)
186 (Supplementary Data 2). Similar to the metabolomic analysis, PCA readily separated the
187 proteome of the late isolates from that of the early isolates, suggesting that changes in
188 metabolite profiles might be rooted in the proteome (Fig. 3a, b). Most of the early and some
189 of the late proteomes colocalized with the reference strain PAO1, indicating little or no
190 changes in proteome allocation (Fig. 3a, b). However, the proteome of the late isolates of
191 lineages DK12, DK17, DK36, and DK55 separated from the respective early strains to form a
192 cluster of adapted proteomes (Fig. 3a, b). Notably, the DK03 strains formed an independent
193 cluster, indicative of a lineage specific proteomic signature (Fig. 1a and 3a, b).

194 A similar relationship between the proteomes is obtained through HCA, specifically when
195 considering the 235 differentially expressed proteins (late *vs* early comparison) belonging to
196 the Clusters of Orthologous Groups (COG) categories involved in metabolism (Fig. 3c). The
197 adapted metabotypes DK12, DK36 and DK55 and DK17 (cluster B) separate from the naïve
198 metabotypes (cluster A) supporting our hypothesis that metabolic specialization is likely
199 rooted in changes in expression of proteins involved in cellular metabolism (Fig. 3c). Notably,
200 cluster B is characterized by a higher number of differentially expressed proteins in the
201 categories of amino acids and lipid metabolism, and energy production and conversion
202 relative to cluster A (Fig. 3d and Fig. S1a). Similarly, several categories of proteins involved in
203 the metabolism of amino acids, fatty acids, and sugars are statistically enriched in naïve and
204 adapted clone types (Fig. S1b) providing a molecular explanation for the altered hierarchy of
205 assimilation of the carbon sources and the reduced growth rate of the late adapted
206 metabotypes (Fig. 2c, d).

207 Although late strains of DK12, DK36, DK55 belong to different metabotypes, their proteomes
208 move in the same direction (Fig. 3a-c). This indicates that largely similar proteomes can
209 sustain distinct metabolic configurations which ultimately depend on the metabolic fluxes
210 thorough specific pathways and on their regulation. We note that, in the case of strain DK17_L
211 (cluster B) (Fig. 3a-c), although our metabolomic analysis did not detect any major metabolic
212 rewiring (Fig. 2a, b), its proteome reorganization could be related to other metabolic
213 processes which were not analysed in our study.

214 Interestingly, several enzymes belonging to the Entner-Doudoroff/Embden-Meyerhof-
215 Parnas/Pentose Phosphate (EDEMP), and tricarboxylic acid (TCA) cycle pathways are up-
216 regulated in the early and late strains relative to PAO1, indicating that enzymes involved in
217 central carbon metabolism converge to a configuration that is optimal for exploiting the
218 airway's resources (Fig. 3e and S2). For example, our metabolomic data show that several late
219 strains (belonging to metabotypes 2 and 3) exhibit increased glucose assimilation, which is in
220 agreement with the increased expression of pathways involved in glucose assimilation
221 (enzymes 3, 11, 12, 18) (Fig. 3e). Similarly, fumarate hydratase (enzyme 33) together with the
222 enzymes involved in Trp, Phe and Tyr catabolism (enzymes 65 and 66) shows increased
223 expression, likely to better accommodate the increased assimilation of amino acids
224 catabolized through the TCA cycle (Fig. 3e). This result is corroborated by the changes in
225 expression (both increased and decreased) in late *vs* early strains of several enzymes involved
226 in amino acid, glucose, and lactate catabolism, and of their respective transporters (Fig. 3e).
227 This proteome configuration supports the hypothesis that overflow of amino acids through
228 central carbon metabolism might be the cause of increased pyruvate secretion in the late
229 strains of DK12, DK36 and DK55 (Fig. 2d and 3e).

230

231 *Changes in virulence traits during within patient evolution*

232 To evaluate the relationship between metabolic specialization and virulence, we analysed
233 which differentially expressed proteins were enriched when comparing late *vs* early isolates.
234 Interestingly, most of the changes (based on their KEGG and GO categories) are directed
235 towards adaptation to the infection environment, redox balance and virulence (Fig. 4a and
236 S1b). For example, most of the lineages show expression changes in phenazine biosynthesis

237 (KEGG) and secondary metabolite(s) biosynthetic process (GO), both of which are deeply
238 involved in redox-balance, cell homeostasis, metabolism and virulence [39,40].

239 Several changes in protein expression are already apparent in early strains relative to PAO1
240 indicating a different response of clinical strains to the airway-like conditions accompanying
241 growth in SCFM2 (Fig. 4a). Specifically, early strains show increased expression of proteins
242 involved in alginate production, hydrogen cyanide (HCN), phenazine biosynthesis and PQS
243 (the *Pseudomonas* quinolone signal), and decreased expression of proteins involved in flagella
244 biogenesis, lipopolysaccharide (LPS) O-antigen metabolism and pyoverdine production, which
245 are all hallmarks of an acute infection phenotype (Fig. 4b). Early stage colonization and acute
246 infection are thought to require expression of several virulence factors promoting host tissue
247 injury and immune response impairment [41]. By contrast, the adapted metabotypes - and
248 specifically strains belonging to cluster B (DK12, DK17, DK36 and DK55) - show convergent up-
249 regulation of proteins related to alginate, phenazine, PQS and the type VI secretion system
250 (T6SS), suggesting that metabolism plays an active role in regulating virulence and the chronic
251 infection phenotype (Fig. 4c and S3). Reduced virulence and cytotoxicity is advantageous for
252 long-term infection and the establishment of a persistent infection [42]. Interestingly, the DK12
253 late strain also shows lower expression (-3-fold) of the type III secretion system (T3SS) toxin,
254 ExoT, which is known to play a role in preventing phagocytosis, in the induction of cytoskeletal
255 reorganization, and in host cell apoptosis [15]. Overall, the identified pattern of proteomic
256 changes suggests that the early isolates manifest reduced immunogenicity relative to PAO1,
257 with an even greater reduction being associated with the late isolates. This is consistent with
258 their persistence during CF airway infections [42].

259

260 *aceE and aceF mutations leads to metabolic specialization and impaired virulence*

261 From the previously published genome sequences [36], we searched for mutations in the
262 genome of each clinical isolate which might explain the secretion of pyruvate and the
263 metabolic specialization of late isolates. In particular, we focused on those genes encoding
264 the phospho*enol*pyruvate-pyruvate-oxaloacetate node (Fig. 3e), since such mutations might
265 be expected to lead to elevated pyruvate secretion. This led to the identification of mutations
266 in genes encoding the pyruvate dehydrogenase complex (PDHc), *aceE* and *aceF*, in late strains

267 of DK12 and DK36, respectively. The PDHc catalyses the conversion of pyruvate to acetyl-CoA,
268 connecting sugar metabolism with the TCA cycle (Fig. 3e). Interestingly, the *aceE* and *aceF*
269 genes are candidate pathoadaptive genes, suggesting positive selection for such mutations in
270 pwCF [36]. In our strain collection of 474 isolates from 34 pwCF [36], we identified the presence of
271 18 different *aceE*/*aceF* mutations (4 indels and 14 SNPs, of which 3 were silent) in 18 separate
272 lineages. These lineages were present in more than half of the patients, supporting the
273 hypothesis that modulation of the PDHc might be selected for during airway infections (Fig.
274 S4). Moreover, *in-situ* expression of the *aceE* and *aceF* genes is reduced in sputum samples
275 collected from chronically infected pwCF [36,43]. This suggests an undescribed role of the PDHc
276 activity which connects central carbon metabolism and pathogenicity during infection.

277 The DK12_L and DK36_L strains contained a +TCCC duplication at position 813 in *aceF*, and a
278 T→C transition at position 551 in *aceE*, respectively (Fig 5a). To evaluate the contribution of
279 these mutations to the bacterial phenotype, independent of the underlying historical
280 contingency of the clinical strains, we generated recombinant PAO1 derivative strains
281 containing the same mutations. The *aceF* mutation leads to a frameshift starting from Lys 273,
282 whereas the *aceE* mutation leads to a Phe→Ser amino acid change. The recombinant *aceE*
283 and *aceF* mutant strains show reduced growth rate (Fig. 5b) and increased secretion of
284 pyruvate (maximal pyruvate accumulation by the *aceE* mutant was 0.5 mM, whereas for *aceF*,
285 the value was 13 mM) (Fig. 5c). By comparison, maximal pyruvate accumulation by the
286 DK12_L and DK36_L late strains was 8.5 mM and 4.6 mM, respectively (Fig. 2d). The PAO1-
287 derived *aceE* mutant strain clearly has a milder phenotype (a smaller reduction in growth rate
288 and lower pyruvate secretion) compared with the *aceF* mutant strain, suggesting partial
289 functionality of the PDHc. Indeed, we were able to fully restore the growth phenotype of the
290 *aceE* strain by supplementing the bacterial culture with acetate (to replenish the pool of
291 acetyl-CoA), whereas this only partially restored growth in the *aceF* mutant strain (Fig. 5b).
292 These data confirm that the frameshift in *aceF* has a much greater impact on PDHc activity
293 than the SNP in *aceE*. Surprisingly, phenotypes such as biofilm formation, motility, redox
294 susceptibility, pyoverdine production, and antibiotic susceptibility showed no statistical
295 difference between the PAO1 wild-type strain and the *aceE* and *aceF* mutant strains, except
296 for a slight decrease in twitching motility and mildly increased tobramycin susceptibility (Fig.
297 S5).

298 To characterize the effect of the *aceE* and *aceF* mutations more broadly, we performed whole
299 cell proteomics on the *aceE* and *aceF* recombinant strains (and on the PAO1 progenitor) in
300 presence and absence of acetate. In total, we quantified 3246 proteins and identified 449 as
301 differentially expressed in at least one comparison of either mutant *vs* wild-type strain or of
302 mutant strain in presence *vs* absence of acetate (Supplementary Data 3). In the absence of
303 acetate, the proteome of the *aceE* and *aceF* mutant strains was clearly different compared
304 with that of PAO1 (Fig. 5d). PC1, which encompasses >50% of the variance in the dataset,
305 separated the *aceF* strain proteome from that of PAO1, whereas the proteome of the *aceE*
306 mutant was more similar to that of PAO1, separating along PC2 (accounting for just 20% of
307 the total variance in the dataset, Fig. 5d). As previously noted, supplementation of the growth
308 medium with acetate benefited both the *aceE* and *aceF* strains, with both proteomes moving
309 closer to that of PAO1 (Fig. 5d). This effect was greater in the *aceF* mutant strain, where
310 growth in acetate decreased the number of up-regulated proteins (cf. PAO1) by more than
311 half (from 301 to 126) (Fig. 5e). Unsurprisingly, the expression of several enzymes involved in
312 pyruvate and acetyl-CoA metabolism (e.g., lactate dehydrogenase (41), acetyl-coenzyme A
313 synthetase (6), citrate synthase (28)) return to wild-type levels following the addition of
314 acetate (Fig. 5f and S6a). Similarly, for the clinical isolates DK12_L and DK36_L, the categories
315 of proteins involved in amino acid/lipid metabolism and energy conversion presented the
316 largest number of differentially expressed proteins (Fig. S6b). Moreover, proteins involved in
317 terpene, propionate, isoprenoid and branched-chain amino acid metabolism (all of which are
318 directly connected to pyruvate and acetyl-CoA metabolism) were statistically enriched in the
319 PAO1-derived *aceF* mutant, indicating a reorganization of both central and peripherical
320 pathways to cope with reduced synthesis of acetyl-CoA (Fig. S6c). The PAO1-derived *aceE*
321 mutant strain also shows an extreme down-regulation of the oxygen-sensing transcriptional
322 regulator Dnr, which is known to be required for denitrification but also regulates acetate
323 metabolism and the T6SS [44–46]. This mirrors the down-regulation seen specifically for cluster B
324 of the clinical isolates (Fig. 3c), which may suggest a role for Dnr down-regulation in metabolic
325 specialization (Fig. S6d).

326 Importantly, the *aceE* and *aceF* mutant strains show increased expression of proteins involved
327 in alginate production and T6SS, as well as decreased expression of proteins involved in the
328 T3SS, including the secreted factor ExoT (in strains *aceF* and DK12_L) (Fig. 5g and

329 Supplementary Data 3). This indicates that the *aceE* and *aceF* mutations contribute to the
330 expression profile of virulence determinants shown by the late clinical isolates of DK12 and
331 DK36 (Fig. 4, 5g and Supplementary Data 3).

332

333 *Pyruvate dehydrogenase mutations modulate pathogenicity in ALI culture infections*

334 To test whether the secretion of pyruvate and the reduced expression of virulence
335 determinants in the PAO1-derived *aceF* and *aceE* mutant strains lead to reduced infectivity,
336 we performed host-bacteria infections using an ALI infection model system. This model
337 system is composed of mucociliated differentiated airway epithelial cells which represent the
338 airways and provides insights into the host response including epithelial damage and
339 recruitment of the immune system. Overall, the *aceF* mutant strain displayed a broad
340 suppression of virulence, including reduced epithelium damage and innate immune
341 recognition during the infection (Fig. 6). The transepithelial electrical resistance (TEER) which
342 quantifies the integrity and permeability of the epithelial layer, LDH release which quantifies
343 the epithelium cellular damage, and the bacterial count which quantifies the growth and
344 penetration of the bacteria through the epithelium to the basolateral side of the ALI
345 transwells, all showed reduced values after 14 h of infection by the *aceF* mutant, compared
346 with the PAO1 reference strain (Fig. 6a). This is in line with the behaviour of a *ΔpscC* mutant
347 strain defective in T3SS, which also shows severely reduced virulence (Fig. 6a). By contrast,
348 the *aceE* strain elicited epithelial damage similar to PAO1, indicating that the mutation does
349 not influence bacterial penetration (Fig. 6a). This is consistent with the proteomic analysis
350 showing no significant differential expression in this strain for proteins involved in T3SS which
351 is the leading cause of epithelial damage (Fig. 5g). However, both the *aceE* and *aceF* strain
352 together with the *ΔpscC* mutant strain elicit lower interleukin 8 (IL-8) release, a cytokine that
353 is secreted by epithelial cells and is necessary for the recruitment of the immune system at
354 the site of infection (Fig. 6b). Such reduced recognition from the epithelial layer of the *aceE*
355 and *aceF* strains might depend on the secretion of bacterial pyruvate, which is known to
356 mediate the inflammatory response in both the epithelium and the immune cells [34,35,47]. These
357 results are corroborated by confocal microscopy data, which show a similar colonization
358 profile on the airway epithelium of the PAO1 and *aceE* strains, and of the *aceF* and *ΔpscC*
359 respectively. It is worth noting that nuclei shedding, seen as nuclei (in blue) being pushed to

360 the apical side of the epithelium (in red), was observed only for PAO1 and not for the *aceE*
361 mutant strain (Fig. 6c), which may suggest a slight reduction in the aggressiveness of the
362 infection. This mechanism of reduced cellular damage and reduced immunogenicity seems
363 not to depend on the growth defect associated with the *aceF* strain, since the *ΔpscC* strain
364 shows comparable aggressiveness to the *aceF* mutant strain but a wild type-like growth rate.

365 Importantly in our longitudinal collection of clinical *P. aeruginosa* strains, 18 different lineages
366 (specific clone types obtained from different pwCF; 89 isolates) harboured mutations in the
367 *aceE* and *aceF* genes and/or additional mutations in T3SS genes [36]. In 9 lineages, PDHc
368 mutations are present alone or anticipate additional T3SS mutations. In 7 lineages, T3SS
369 mutations precede PDHc mutation or both systems are mutated at the same time (4 lineages)
370 already in the first isolate of the lineage (Fig. S7). Altogether these results suggest a role for
371 the *aceE* and *aceF* mutations prior to those affecting the T3SS. Moreover, they provide direct
372 evidence of the contribution of metabolism to bacterial virulence and to the persistence
373 phenotype.

374

375 **Discussion**

376 Metabolism constitutes a central process which is specifically regulated and optimized
377 according to the nutritional resources available and the phenotypic requirements of the cell.
378 Several studies have shown that metabolic specialization occurs in clinical isolates of *P.*
379 *aeruginosa* [5,9,23,24,48]. However, little is known about whether this metabolic specialization is
380 simply an accommodation for other significant fitness gains, i.e. metabolic compensation for
381 phenotypes with high fitness cost, or whether it is specifically selected to enable increased
382 persistence in the host.

383 By analysing a range of longitudinal clinical isolates of *P. aeruginosa*, we found that all
384 infection lineages underwent a substantial metabolic rewiring. This includes CF-specific
385 patterns of carbon source (amino acids, sugars and organic acids) assimilation and
386 fermentation (acetate secretion). These metabolic changes, in turn, are associated with
387 changes in proteome allocation potentially driven by mutations in metabolic genes. Adapted
388 strains harbouring mutations in genes (*aceE* and *aceF*) encoding the PDHc are characterized
389 by a chronic-like phenotype (T3SS down-regulation, up-regulation of the T6SS, phenazines,

390 the alginate biosynthetic pathway, and slow growth) suggesting that these mutations confer
391 a selective advantages in the host [4]. Moreover, adapted strains secrete large amounts of
392 pyruvate, which is an important mediator of inflammation in the host [34]. Reconstitution of
393 clinical *aceE* and *aceF* mutations in a defined laboratory strain (PAO1) revealed that these
394 mutations elicit reduced stimulation of the immune system and reduced epithelial layer
395 penetration when compared with the isogenic wild-type progenitor strain (PAO1), which
396 exhibits a highly virulent phenotype similar to that associated with acute infection. These
397 findings are consistent with the notion that strains with reduced virulence are selected during
398 within-patient evolution in pwCF to reduce host tissue damage and limit the activity of the
399 immune system [49]. Such reduced aggressiveness in the *aceF* mutant strain appears to be
400 mediated by lower expression of the T3SS effector, ExoT, which induces apoptosis in host cells
401 [15,16]. This is consistent with previous studies showing that mutations in the PDHc-encoding
402 genes lead to repression of T3SS in *P. aeruginosa* [30,50]. Mutations in the enzyme *iso*citrate
403 lyase, involved in the glyoxylate shunt of the TCA cycle, have also been associated with
404 reduced T3SS activity, suggestive of a direct correlation of metabolism to virulence [28]. This is
405 the case for the DK15 late isolate in our collection, which shows reduced expression of
406 *iso*citrate lyase together with suppression of the ExoT exotoxin. Importantly, *aceE* and *aceF*
407 mutations mostly precede mutations in the T3SS-encoding genes, indicating a fundamental
408 and broader role of the PDHc mutations during evolution in the host. Moreover, the diversity
409 of *aceE* and *aceF* mutations indicate that the activity of the PDHc can be fine-tuned
410 accordingly to the specific host environment and consequently lead to different infection
411 outcomes. Indeed, while the *aceE* mutant strain (carrying just a SNP) shows comparable
412 aggressiveness to PAO1 but reduced recruitment of the immune system (IL-8 secretion), the
413 *aceF* mutant strain (carrying a frameshifting indel) combines the effect of the reduced
414 aggressiveness and that of the reduced immune recruitment.

415 It is worth noting that pyruvate, in addition to its crucial role as intermediate of central carbon
416 metabolism, is a potent scavenger of ROS which use has been suggested as an anti-
417 inflammatory treatment in several diseases [33,47]. Due to the sustained activation of neutrophils
418 and other defects in the homeostatic processes of pulmonary epithelia in CF airways, an
419 abnormal flux of ROS is present which can be alleviated by the bacterial pyruvate secretion [51].
420 It has been shown that treatment of human lung epithelial cells with pyruvate reduces the

421 inflammatory response by reducing the production of IL-8 [52,53]. It induces a potent shutdown
422 of the response to LPS in dendritic cells [54] and reduces alveolar tissue destruction in a COPD
423 model system [55]. Similarly, inhibition of the PDHc and redirection of the pyruvate flux has been
424 suggested both as a potential anti-inflammation therapy for chronic metabolic diseases [56] and
425 as a cancer treatment [57]. Moreover, fine-tuning of the flux through the mitochondrial PDHc in
426 macrophages and dendritic cells is key for regulating their polarization and thus the balancing
427 between pro- and anti-inflammatory responses [35,58]. LPS-induced polarization of macrophages
428 is prevented by pharmacological inhibition of pyruvate import into the mitochondria [59].
429 Moreover, flux through the PDHc controls the production of the antibacterial
430 immunometabolite itaconate by macrophages [60–63].

431 The metabolic specialization and specifically the PDHc dysregulation seen in the clinical
432 isolates may, therefore, serve as a mechanism for ensuring active pyruvate secretion and
433 suppression of the immune system by a mechanism of cross-feeding. The evolutionary benefit
434 of such a mechanism of host-pathogen crosstalk during persistent infections may explain why,
435 in many cases, ROS produced in the CF airways appear to select for metabolic specialization
436 in *P. aeruginosa* [64]. Moreover, the consequent phenotypic change of metabolically adapted
437 strains limits epithelial damage to avoid any further inflammation. Indeed, changes in T3SS,
438 T6SS, phenazines, alginate biosynthesis, and growth physiology are all hallmarks of a
439 transition from an acute (high virulence) to a chronic (low virulence) phenotype which are
440 specifically selected for during colonization of pwCF [4,49]. These combined mechanisms of
441 cross-feeding and reduced virulence in turn promote persistence in the host by a change in
442 the infection microenvironment which can benefit the entire population of infecting bacteria.
443 Moreover, they can provide a rationale for the broad accumulation and maintenance of PDHc
444 mutations in *P. aeruginosa* clinical CF isolates and the reduced expression of the PDHc in
445 sputum samples [36,43]. This suggests a highly complex and near universal role of the pyruvate
446 node in regulation of both host and pathogen (and their respective functions *in vivo*) through
447 a conserved central metabolite. Such a mechanism might be engaged years before the
448 development of antibiotic resistance, because of its high relevance for the establishment of a
449 chronic phenotype.

450 The mechanism of metabolic specialization presented here is only one of many different
451 mechanisms that *P. aeruginosa* might use for long-term survival in the host. However, the

452 connection between metabolic behaviours and virulence phenotype (acute or chronic) are
453 still poorly characterized, limiting our capacity to design treatments that counteract such
454 processes. While our work focuses on a limited collection of clinical strains, a systematic
455 analysis of the heterogeneous populations infecting pwCF is necessary to fully evaluate the
456 role of metabolic specialization in persistence. Designing new methods e.g. for high-
457 throughput metabolomics analyses under *in vivo* like conditions, such as those recreated by
458 ALI or organoid cultures [65] which go beyond the limitation of laboratory conditions, will allow
459 the characterization of new persistence mechanisms by clarifying the relationship between
460 the host, the pathogen and other microbial species of the host microbiota. Still, it is important
461 to note that the pyruvate secretion and the associated phenotypic changes described here
462 might be beneficial not only for the PDHc mutated population but also for other nearby "wild-
463 type" cells, since they alleviate the airway inflammation and limit the recruitment of the
464 immune system. Importantly, metabolic specialization might be equally relevant in other
465 persistent infections such as those caused by *Escherichia coli*, *Staphylococcus aureus* and
466 *Mycobacterium tuberculosis* which are similarly threatening and difficult to tackle [2]. Finally,
467 understanding specific mechanisms linking metabolism, energy balance and virulence, and
468 most importantly how the relationship between the host and the pathogen changes during
469 an infection, could provide new opportunities for more efficient and/or complimentary
470 treatments, beyond the classical antibiotic treatment, which are greatly needed.

471

472

473 **Methods**

474 *Strains and media*

475 The collection of clinical isolates used in this study is a subset of the collection published in
476 Marvig et al., (2015) and Bartell et al., (2019) [8,36]. The local ethics committee at the Capital
477 Region of Denmark (Region Hovedstaden) approved the use of the stored *P. aeruginosa*
478 isolates (registration number H-21078844). For information about specific clinical isolates,
479 see Table S1.

480 For construction of *aceE, aceF* and *ΔpscC* mutant strains, derivatives of pACRISPR were
481 constructed with the Uracil Specific Excision Reagent (USER) cloning [66]. The plasmids and
482 primers used are listed in Table S1 and S2 respectively. Target DNA fragments were amplified
483 from gDNA of clinical strains DK12 Late and DK36 Late using the Phusion U polymerase kit
484 (Thermo Fisher Scientific, USA). For the *ΔpscC* mutant strain primers were designed to create
485 matching short overlaps between the DNA fragments that should be stitched together in the
486 final plasmid. The resulting products were treated with FastDigest DpnI enzyme (Thermo
487 Fisher Scientific, USA) and ligated with the USER® Enzyme (New England Biolabs, USA). PCR
488 was performed on random *E. coli* DH5alpha colonies using OneTaq® 2X Master Mix (New
489 England Biolabs, USA) to confirm the correct insertions and further sequenced with Sanger
490 method (Eurofins Scientific, Luxembourg). *aceE, aceF* and *ΔpscC* mutations in the genome of
491 *P. aeruginosa* PAO1 were introduced using the previously developed CRISPR-Cas9 system and
492 following the indicated protocol [67] with the addition of 0.2% arabinose in the growth medium
493 during transformation. To confirm the presence of desired mutations, PCR fragment of the
494 genome around the mutations was amplified and sequenced with Sanger sequencing
495 (Eurofins Scientific, Luxembourg). To perform confocal microscopy analyses, strains were
496 tagged with GFP using four parental mating using a mini Tn7 delivery-method [68] but for strains
497 *aceE* and *aceF* with the additional supplementation of 5 mM acetate to ensure growth of
498 PDHc dysregulated target strains. Transformants were identified by green fluorescence and
499 validated by comparing growth rate to the untagged target strain.

500 Bacteria were grown in Synthetic Cystic Fibrosis Media 2 (SCFM2) [69]. To reduce viscosity and
501 allow for HPLC analysis, DNA and mucins were excluded [70]. Cultures were grown at 37 °C and
502 250 rpm.

503

504 *Dynamic exo-metabolomics analyses*

505 Sampling of supernatants was performed in 96-well deep well plates (Cat. No. 0030502302;
506 Eppendorf, Hamburg, Germany) with an air:liquid ratio of 1:1 using a high-throughput
507 dilution-based growth method as previously described [71]. Immediately before sampling, OD_{600}
508 of the cultures were measured in a Synergy™ MX microtiter plate reader (BioTek Instruments
509 Inc., Winooski, VT, USA). Supernatants were stored at -80 °C until HPLC-analysis. For organic

510 acids and sugars (glucose, lactate, formate, acetate and pyruvate), a Dionex Ultimate 3000
511 system (Thermo Scientific,Waltham, United States) with a HPx87H ion exclusion column (125-
512 0140, Aminex, Dublin, Ireland), equipped with a guard column (125-0129, BioRad, Hercules,
513 California, United States) and guard column holder (125-0131, BioRad, Hercules, California,
514 United States) was used. Samples were injected with an injection volume of 20 μL and eluted,
515 using a 5 mM H_2SO_4 mobile phase, at an isocratic flow of 0.6 mL min^{-1} at 45 °C for 30 min.
516 Pyruvate was analysed by UV detection at a wavelength of 210 nm, using a System Gold 166
517 UV-detector (Beckman Coulter, Brea, United States), while the rest of the metabolites were
518 analysed by RI detection, using a Smartline RI detector 2300 (KNAUER Wissenschaftliche
519 Geräte, Berlin, Germany). For amino acids (aspartic acid, glutamic acid, serine, histidine,
520 glycine, threonine, arginine, alanine, tyrosine, valine, phenylalanine, isoleucine, leucine,
521 lysine and proline), 20 μL of the thawed sample was diluted 1:10 by mixing with 80 μL
522 Ultrapure MilliQ water and 100 μL of internal standard (20 μg/mL 2-aminobutyric acid and
523 sarcosine) before injection of 56.5 μL into the instrument. Prior to injection into the column,
524 derivatization of amino acids was performed in the HPLC-instrument by automatic mixing
525 with the following eluents: (i) 0.5% (v/v) 3-mercaptopropionic acid in borate buffer 0.4 M at
526 pH 10.2; (ii) 120 mM iodoacetic acid in 140 mM NaOH; (iii) OPA reagent (10 mg/mL *o*-
527 phtalaldehyde and 3-mercaptopropionic acid in 0.4 M borate buffer); (iv) FMOC reagent (2.5
528 mg/mL 9-fluorenylmethyl chloroformate in acetonitrile); and (v) buffer A (40 mM Na_2HPO_4,
529 0.02% (w/v) NaN_3 at pH = 7). Following derivatization, the samples were separated
530 isocratically on a Dionex Ultimater 3000 HPLC with fluorescence detector (Thermo Scientific,
531 Waltham, United States) through a Gemini C18 column (00F-4439-E0, Phenomenex, Værløse,
532 Denmark) equipped with a SecurityGuard Gemini C18 guard column (AJ0-7597, Phenomenex,
533 Værløse, Denmark) with 5 mM H_2SO_4 at a flowrate of 1 mL min^{-1} at 37 °C for 31 min. Amino
534 acids were detected using an UltiMate™ 3000 Fluorescence variable wavelength UV detector
535 (FLD-3400RS, Waltham, Massachusetts, United States).

536

537 *Proteomic analyses*

538 To maintain a 1:1 air:liquid ratio, as in the metabolomic analysis, 25 mL SCFM2 cultures were
539 inoculated from ON cultures in 50 mL Falcon tubes at OD_{600} of 0.05 and then incubated in an
540 orbital shaker at 37 °C and 250 rpm until sampling by centrifugation at mid-exponential phase.

541 Five biological replicates were analysed for PAO1 and the clinical isolates while three
542 biological replicates for the PAO1 derivative strains *aceE* and *aceF* both in presence and
543 absence of 5 mM acetate. Pellets were washed twice with PBS and stored at -80C until protein
544 extraction. No specific preparation or enrichments were performed to identify secreted
545 proteins. For experiment with clinical isolates, protein extraction was done in Lysis buffer A
546 (100 mM Tris, 50 mM NaCl, 1 mM tris(2-carboxyethyl)phosphine (TCEP), 10% glycerol, pH =
547 7.5) with *cOmplete Mini protease inhibitor* (Roche) by sonication at amplitude 10 for 3x 10s
548 cycles with 20s cooling between, followed by acetone precipitation and resuspension in Lysis
549 buffer B (6 M Guanidinium hydrochloride, 5 mM TCEP, 10 mM chloroacetamide, 100 mM Tris–
550 HCl, pH = 8.5). For experiment with PAO1 derivative mutant strains, protein extraction was
551 done in Lysis buffer B by bead beating with 3-mm zirconium oxide beads at 99 °C for 5 min. in
552 a Tissuelyzer (Retsch, MM 400) at 25 Hz, then boiled, still at 99 °C, in heat block (Eppendorf
553 Thermomixer C) for 10 min. while shaking/mixing at 2000 rpm. In both cases, protein
554 concentrations were determined by micro BCA™ Protein Assay Kit (Thermo Scientific, prod
555 #23235) and 100 μg protein was used for trypsin digest in Trypsin/Lys-C Buffer (0.1 μg/μL
556 trypsin, 50 mM Ammonium Bicarbonate). The reaction was stopped by addition of 10 μL 10%
557 TFA and samples were desalted by stagetipping with C18 filter plugs (Solaµ HRP 2 mg/1 ml 96
558 well plate, Thermo Scientific). Peptide samples were stored in 40 μL of 0.1% Formic acid at 4
559 °C until LC-MS analysis.

560 For the experiment with clinical isolates, LC-MS/MS was carried out using a CapLC system
561 (Thermo Fisher Scientific Inc., Waltham, USA) coupled to an Orbitrap Q-exactive HF-X mass
562 spectrometer (Thermo Fisher Scientific Inc., Waltham, USA). The first samples were captured
563 at a flow of 10 μL/min on a precolumn (µ-pre-column C18 PepMap 100, 5 μm, 100 Å) and then
564 at a flow of 1.2 μL/min. Peptides were separated on a 15 cm C18 easy spray column (PepMap
565 RSLC C18 2 µm, 100Å, 150 µmx15cm). The applied gradient went from 4% acetonitrile in water
566 to 76% over a total of 60 minutes. MS-level scans were performed with Orbitrap resolution
567 set to 60,000; AGC Target 3.0e6; maximum injection time 50 ms; intensity threshold 5.0e3;
568 dynamic exclusion 25 sec. Data dependent MS2 selection was performed in Top 20 Speed
569 mode with HCD collision energy set to 28% (AGC target 1.0e4, maximum injection time 22 ms,
570 Isolation window 1.2 m/z). For the experiment with the *aceE* and *aceF* mutant strains,
571 peptides were loaded onto a 2 cm C18 trap column (ThermoFisher 164946), connected in-line

572 to a 15 cm C18 reverse-phase analytical column (Thermo EasySpray ES904) using 100% Buffer
573 A (0.1% Formic acid in water) at 750bar, using the Thermo EasyLC 1200 HPLC system, and the
574 column oven operating at 30 °C. Peptides were eluted over a 70 minute gradient ranging from
575 10% to 60% of 80% acetonitrile, 0.1% formic acid at 250 nL/min, and the Orbitrap Exploris
576 instrument (Thermo Fisher Scientific) was run in DIA mode with FAIMS Pro™ Interface
577 (ThermoFisher Scientific) with CV of -45 V. Full MS spectra were collected at a resolution of
578 120,000, with an AGC target of 300% or maximum injection time set to 'auto' and a scan range
579 of 400–1000 m/z. The MS2 spectra were obtained in DIA mode in the orbitrap operating at a
580 resolution of 60.000, with an AGC target 1000% or maximum injection time set to 'auto', and
581 a normalised HCD collision energy of 32. The isolation window was set to 6 m/z with a 1 m/z
582 overlap and window placement on. Each DIA experiment covered a range of 200 m/z resulting
583 in three DIA experiments (400-600 m/z, 600-800 m/z and 800-1000 m/z). Between the DIA
584 experiments a full MS scan is performed. MS performance was verified for consistency by
585 running complex cell lysate quality control standards, and chromatography was monitored to
586 check for reproducibility.

587

588 *Phenotypic characterizations*

589 Growth curves were performed by inoculating 1 μL of ON culture in 149 μL of media, using
590 96-well microtiter plates (Cat. No. 650001; Greiner Bio-One, Kremsmünster, Austria), covered
591 with plate seals (Ref. 4306311, Thermo Fisher Scientific, United Kingdom) and incubated at
592 37 °C and 250 rpm in a BioTek ELx808 Absorbance Microtiter Reader (BioTek Instruments Inc.,
593 Winooski, VT, USA) for 24 - 48 hours. Antibiotic MICs were determined by microdilution. ON
594 cultures were standardized to OD_{600} = 0.5 and diluted 1:2500 to reach 5x 10^5 CFU/mL in fresh
595 SCFM2 media (LB for Azithromycin). Growth assays were performed at increasing antibiotic
596 concentrations and MIC determined based on final OD. Resistance to oxidative stress was
597 measured as the diameter of clearance zones around diffusion disks saturated with 5 μL of
598 fresh 30% H_2O_2 after 24 hours incubation at 37 °C on LB agar plates cast with 3 mL overlay
599 agar containing 100 μL of LB ON culture standardized to OD_{600} = 1. Pyoverdine production was
600 measured as the fluorescence at 400/460 nm excitation/emission on a Synergy H1 Hybrid
601 Multi-Mode Reader (BioTek Instruments, Winooski, VT, USA) of supernatants normalized
602 against OD_{600} of ON cultures in King's B medium. Biofilm formation assay was done as

603 previously described for NUNC peg lids [8] (NUNC cat no. 445497). Motility was measured as
604 the diameter of the motility zone around single colonies deposited in middle layer of 0.3%
605 (swimming), surface layer of 0.6% (swarming) or bottom layer of 1.5% (twitching) LB agar
606 motility plates, after incubation at 37 °C for 24 - 48 hours. For PAO1 wt and *aceEF* mutant
607 strains, pyruvate secretion was determined from supernatants of samples taken after 0, 4, 8
608 and 24 hours of growth in SCFM2. Supernatants were stored at -80C and analysed by the HPLC
609 method also used for exo-metabolomics.

610

611 *Infection of ALI cultures*

612 For the Air-Liquid Interface (ALI) infections the BCi-NS1.1 cells were used [72]. Cells were
613 cultured in Pneumacult-Ex Plus medium (STEMCELL Technologies, 05040) supplemented with
614 Pneumacult-Ex 50x supplement (STEMCELL Technologies, 05008), 96 ng/mL hydrocortisone
615 (STEMCELL Technologies, 07925) and 10 μM Y-27632 ROCK inhibitor (Bio-Techne #1254/10)
616 in a 37 °C, 5% CO_2 humidified incubator. Following expansion, 1.5 x 10^5 cells were seeded onto
617 6.5-diameter-size transwells with 0.4 μm pore polyester membrane inserts (Corning
618 Incorporated, 3470) previously coated with human type I collagen (Gibco, A1048301). ALI was
619 established once cells reached full confluency by removing media from the apical chamber
620 and replacing media in the basolateral chamber with Pneumacult-ALI maintenance medium
621 (STEMCELL Technologies, 05001). Pneumacult-ALI maintenance medium was supplemented
622 with Pneumacult-ALI 10x supplement (STEMCELL Technologies, 05003), Pneumacult-ALI
623 maintenance supplement (STEMCELL Technologies, 05006), 480 ng/mL hydrocortisone and 4
624 μg/mL heparin (STEMCELL Technologies, 07980). ALI cultures were grown in a 37 °C, 5% CO_2
625 humidified incubator for 30 days, with media replacement every 2-3 days. Epithelial
626 polarization was monitored by measurements of the transepithelial electrical resistance
627 (TEER) using a chopstick electrode (STX2; World Precision Instruments). Following 15 days
628 under ALI conditions, the apical surface was washed with PBS every media change to remove
629 accumulated mucus. Biological replicates of bacterial strains were obtained from single
630 colonies on LB agar plates grown ON as precultures in LB and then diluted to an OD_{600} of 0.05
631 before sampling at mid-exponential phase by centrifugation, washing with PBS and
632 resuspending in PBS at a density of 10^5 CFU/mL. Fully-differentiated BCi-NS1.1 cells were
633 inoculated with 10^3 CFU from the apical side, diluted in 10 μL PBS. Control wells were

634 incubated with bacteria-free PBS. Cells were incubated for 14 hours at 37 °C, followed by
635 addition of 200 μL PBS to the apical side and measurement of the TEER. CFUs were
636 determined by platting 10 μL of 6-fold serial dilutions on LB-agar plates in technical triplicates
637 both for the initial inoculum, as well as for the apical and basolateral solutions following TEER-
638 measurements. The basolateral media was also used for measurements of LDH and IL-8
639 release in technical triplicates, using the Invitrogen™ CyQUANT™ LDH Cytotoxicity Assay Kit
640 (Invitrogen, C20301) and Human IL-8/CXCL8 DuoSet ELISA Kit (R&D Systems, DY208)
641 according to the manufacturer´s instructions. BCi-NS1.1 cells on transwell inserts were rinsed
642 once with PBS and fixed by adding 4% (wt/vol) paraformaldehyde (PFA) to both apical and
643 basolateral chambers for 20 min at 4 °C. After washing, cells were permeabilized and blocked
644 for 1 hour with a buffer containing 3% BSA, 1% Saponin and 1% Triton X-100 in PBS. Cells were
645 stained on the apical side with Phalloidin-AF488 (Invitrogen, 65-0863-14) and TO-PRO3
646 (Biolegend, 304008) diluted in a staining buffer (3% BSA and 1% Saponin in PBS) at a 1:500
647 dilution for 2 hours at room temperature. Transwells were removed from their supports with
648 a scalpel and mounted on glass slides with VECTASHIELD® Antifade Mounting Medium (VWR,
649 VECTH-1000). Images were acquired with a Carl Zeiss LSM 510 Confocal Laser Scanning
650 Microscope (40× magnification, 1.3 oil) and analysed using the ImageJ software.

651

652 *Data analysis*

653 (*74*)For exometabolomics, all chromatograms were analysed and used to construct standard
654 curves constructed for absolute quantification of concentrations for all 20 metabolites, using
655 software Chromeleon v7.2.9. All other analysis of exo-metabolomic data was done in JMP Pro
656 15.0. To compare between different strains and media batch-effects, OD_{600} was normalized
657 against final OD_{600} of that strain in the experiment and concentrations were normalized
658 against specific concentrations in SCFM2 controls for each batch. Missing values were
659 replaced with 20% of lowest value detected for any metabolite in any sample. Principal
660 component analysis (PCA) and hierarchical cluster analysis (HCA) were done on $C_{metabolite}$ of all
661 quantified metabolites for 16 samples (8 time-points from biological duplicates) of each
662 strain. PCA was done on covariance using JMP Pro 15.0 software. HCA was performed using
663 the "average" clustering method and "correlation" for distance using the R package pvclust
664 2.2. Reliability of the clusters were analysed by 10,000 bootstraps. Metabolite half-life (OD_{50}),

665 defined as the normalized OD_{600}-value, where 50% of the starting concentration of a
666 metabolite is present, was calculated from the sigmoidal mechanistic growth model
667 (Equation: a(1 – bExp(–cx)) where a = asymptote, b = scale and c = rate) [73]. Differences of
668 metabolic preferences between metabotypes were analysed by comparing the assimilation
669 and secretion profiles between strains using OD_{50} values. The net balance of carbon sources
670 assimilated during the growth was calculated by summing the amount (mM concentration)
671 of assimilated metabolites and subtracting the secreted ones. Metabolomics data are
672 enclosed in Supplementary Data 1.

673 For the experiment with clinical isolates, proteomic raw files were analysed using Proteome
674 discoverer 2.4 software with the following settings: Fixed modifications: Carbamidomethyl (C)
675 and Variable modifications: oxidation of methionine residues. First search mass tolerance 20
676 ppm and a MS/MS tolerance of 20 ppm. Trypsin as enzyme and allowing one missed cleavage.
677 FDR was set at 0.1%. The Match between runs window was set to 0.7 min. Quantification was
678 only based on unique peptides and normalization between samples was based on total
679 peptide amount. For the experiment with mutant strains, raw files were analyzed using
680 Spectronaut™ (version 16.2). Dynamic modifications were set as Oxidation (M) and Acetyl on
681 protein N-termini. Cysteine carbamidomethyl was set as a static modification. All results were
682 filtered to a 1% FDR, and protein quantitation done on the MS1 level. The data was
683 normalized by RT dependent local regression model [74] and protein groups were inferred by
684 IDPicker. In both cases, spectra were matched against the *Pseudomonas aeruginosa* PAO1
685 reference proteome (UniProt Proteome ID UP000002438). In both experiments, any protein
686 that was not quantified in at least 3 of 5 or 2 of 3 biological replicates for all strains were
687 excluded from the analysis. Using JMP Pro 15.0, abundances were normalized by Log_2-
688 transformation and biological replicates used for missing value imputation. PCA Wide was
689 done on correlations using JMP Pro 15.0 and HCA was performed on mean Log_2(abundance)
690 and Log_2(Fold change) for the relevant comparisons. HCA was performed using the "average"
691 clustering method and "correlation" for distance using the R package pvclust 2.2. Reliability
692 of the clusters were analysed by 10,000 bootstraps. Differential expression was determined
693 by two-way ANOVA with Tukey's multiple comparisons test, using GraphPad Prism 9.3.1, and
694 defined as those protein-comparisons where Adjusted *P* value ≤ 0.05 and Log_2(Fold Change)
695 ≥ |0.6|. Enrichment analysis was done using the DAVID Functional Annotation Bioinformatics

696 Microarray Analysis tool from lists of Locus Tags of proteins that were differentially expressed,
697 separated into lists of upregulated and downregulated proteins respectively, for each of the
698 relevant strain-comparisons. The reference genome was set as *Pseudomonas aeruginosa*.
699 Proteomics data are enclosed in Supplementary data 2 and 3.

700 Growth rates and maxOD were calculated in JMP Pro 15.0. Blanks were first subtracted from
701 OD_{600}-measurements and values converted to cm^{-1} (using Greiner dimensions for pathlength).
702 The stationary phase was excluded, and growth rates were calculated by fitting the
703 Exponential 3P model to the exponential phase ($r^2 > 0.99$). Mean ± sd was calculated from
704 biological replicates. GraphPad Prism 9.3.1 was used for statistical analysis of biofilm
705 formation, motility, redox sensitivity, pyoverdine production and MICs (See Figure S5 for
706 details), as well as for ALI infection experiments. ALI data are represented as mean ± SEM.
707 Replicates represent independent experiments performed with cells from different passages.
708 Statistical comparisons were calculated using Two-Way ANOVA for TEER and CFU
709 measurements and One-Way ANOVA for LDH and IL-8 measurements. Statistical significance
710 was considered for p-value < 0.05. All figures were finalized in Adobe Illustrator Artwork 27.0.

711

712 *Data availability*

713 The authors declare that all data necessary for supporting the findings of this study are
714 enclosed in this paper (Supplementary Data 1-3). All genomic data is publicly available
715 through the SRA database and has been published previously by Marvig et al., (2015) [36].

716

717 **Acknowledgements**

718 The work was supported by The Novo Nordisk Foundation (grant number NNF20CC0035580),
719 the UK CF Trust (grant number SRC017) and the Independent Research Fund
720 Denmark/Natural Sciences (grant number 9040-00106B). HKL was supported by the NNF
721 Challenge grant NNF19OC0056411. The Basal Cell Immortalized Non-Smoker 1.1 (BCi-NS1.1)
722 cell line was a kind gift from Professor Ronald G. Cristal (Weil Cornell Medical College, New
723 York, USA).

724

Author contributions

BHP, SM and RLR designed the project. BHP, FBS and IP performed the experiments and verified the data. HKJ provided the strains and the clinical data. MW enabled the proteomic analyses. BHP and RLR wrote the first draft of the paper, which after review by all authors, was revised according to the co-authors' suggestions. All authors approved the final version of the manuscript.

Competing interests

The authors declare no competing interests.

Figures and figure legends

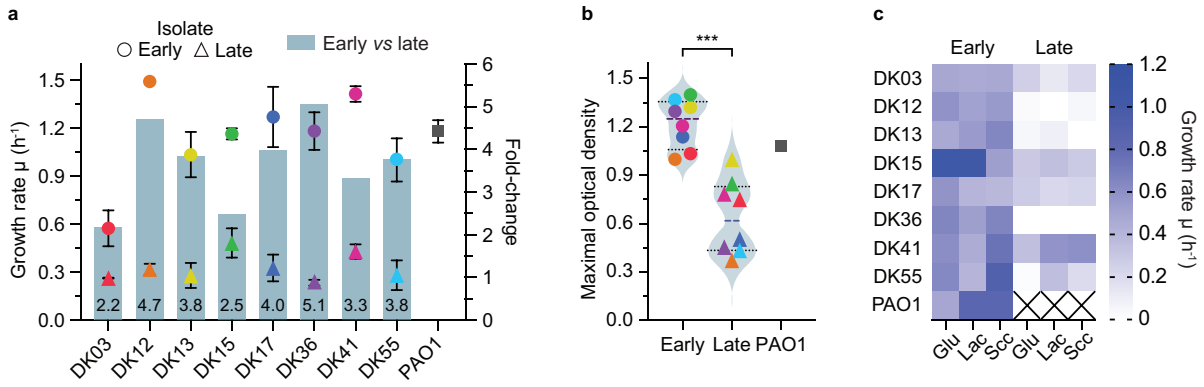

Figure 1: Collection of *Pseudomonas aeruginosa* clinical strains. a) Growth rate (hour^{-1}) of early (circles), late (triangles) and PAO1 (square) strains coloured by their clone type. The fold change of growth rate from early to late is shown as bar chart on the right y axis and as number value at the base of each bar. b) The maximal optical density (maxOD) of all isolates, grouped by early *vs* late comparison. Statistical significance was calculated by Unpaired Welch t-test and indicated as *** ($p < 0.001$). c) Growth rate (hour^{-1}) of each strain in M9 minimal media containing 20 mM of a single carbon source glucose (Glu), lactate (Lac) or succinate (Suc).

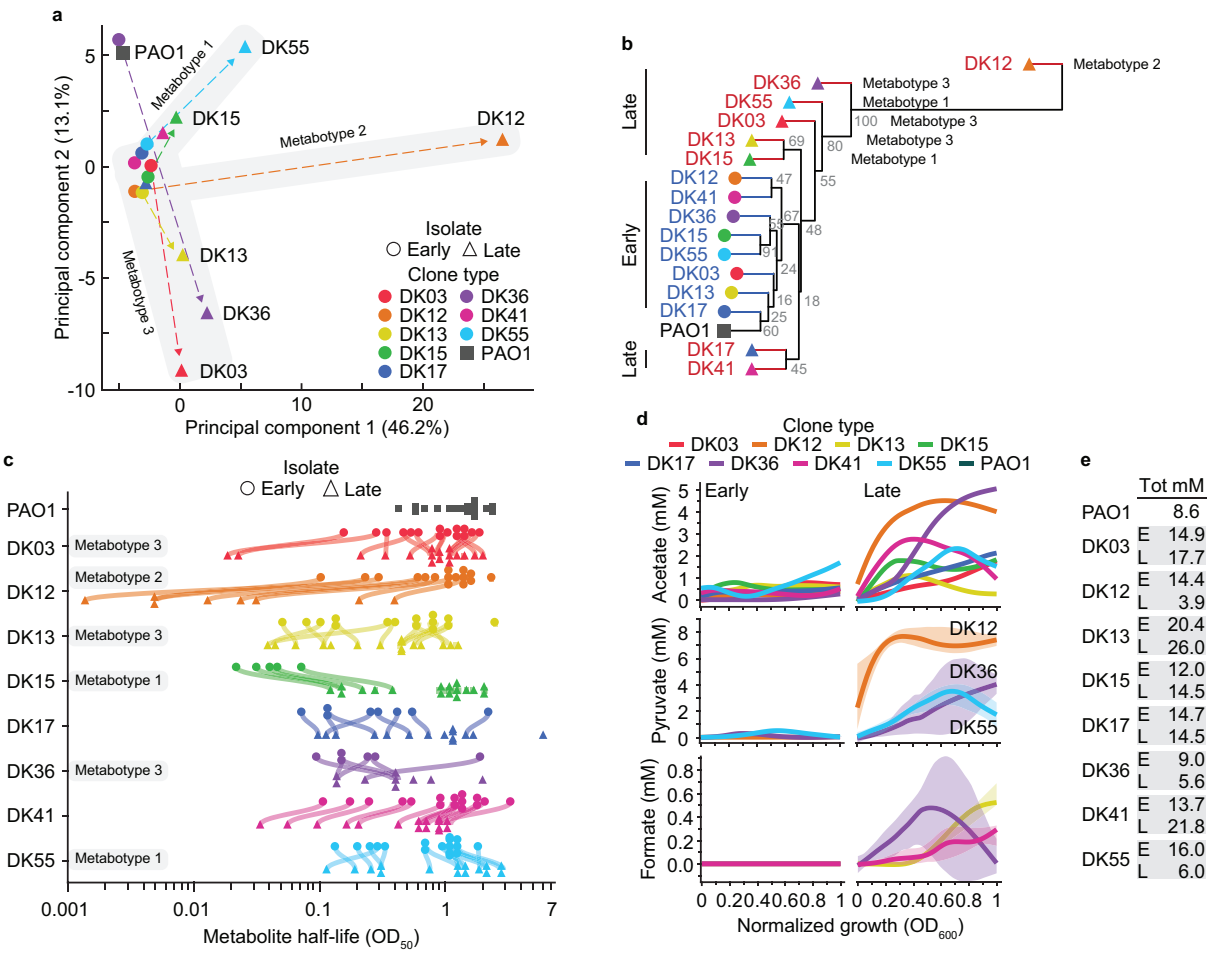

Figure 2: Exo-metabolomics analysis reveals adapted metabotypes. a) PCA showing separation of strains based on their time-resolved exo-metabolomes. Strains are shown as circles (early), triangles (late) and square (PAO1), with dashed arrows indicating most notable trajectories from early to late, coloured by clone type. b) HCA of the exo-metabolomics data, showing a general separation between early and late strains. Branches for early isolates are indicated in blue, late isolates in red and PAO1 in black. Gray values within the branches represent the % of bootstrap values for 10,000 replicates. c) Assimilation hierarchies of the analysed metabolites. Each symbol represents the half-life (OD_{50}) of a specific metabolite while each line connects the same metabolite for each pair of early and late isolates. d) Secretion plots showing variations in the concentration of acetate, pyruvate and formate (mM) relative to normalized growth (OD_{600}). Shaded areas indicate the 95% confidence intervals. e) Table showing the total amount (mM) of carbon sources assimilated for each strain. Secreted metabolites were subtracted from the total to account for their excretion in the medium. Clone types are separated by grey boxes with “E” indicating early and “L” indicating late isolate.

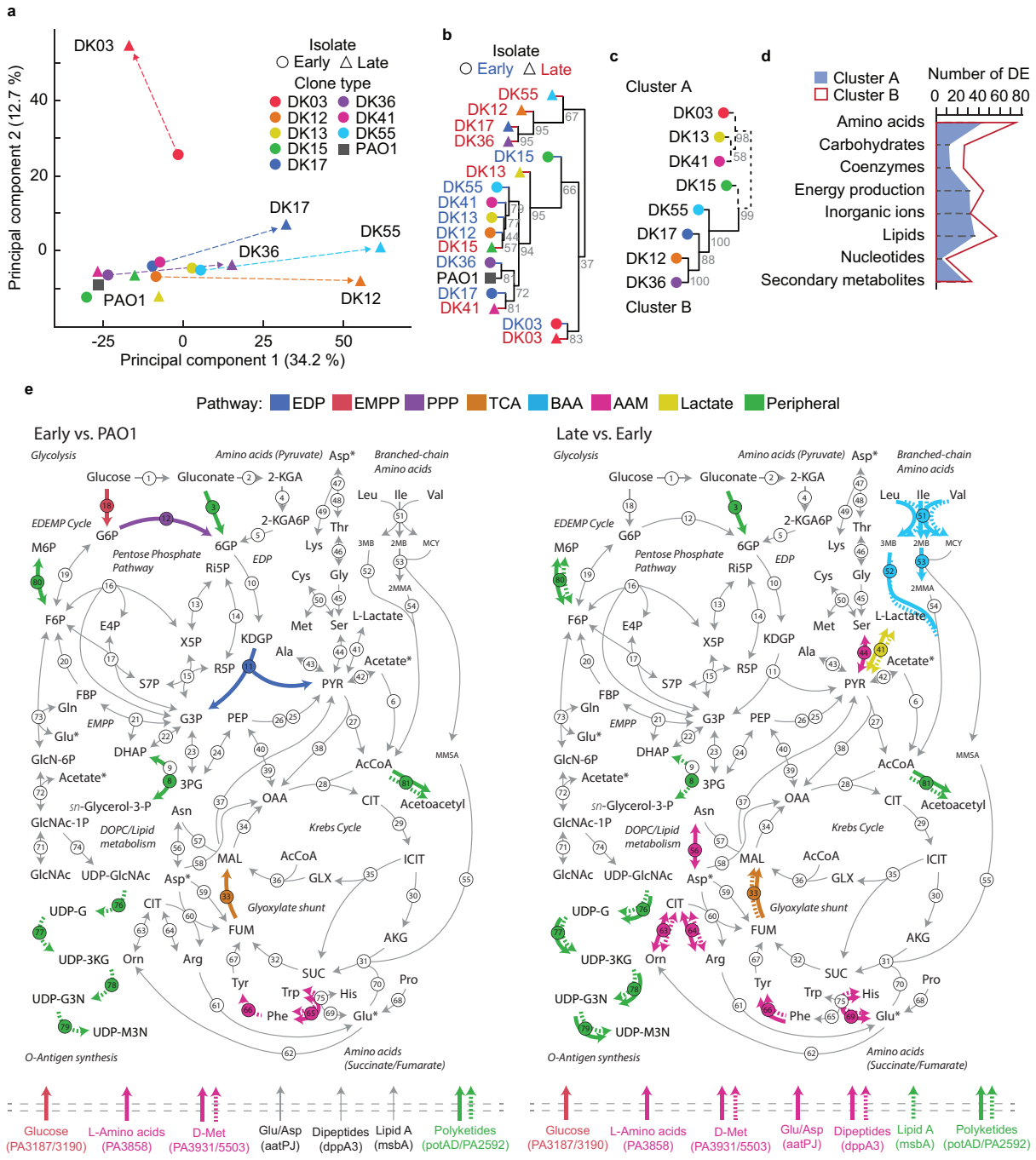

Figure 3: Proteome composition changes support metabolism specialization. a) PCA showing separation of strains based on their mid-exponential proteomes. Strains are shown as circles (early), triangles (late) and square (PAO1), with dashed arrows indicating most notable trajectories from early to late, coloured by clone type. b) HCA of the proteomic data containing 2061 proteins identified, showing a general separation between early and late strains. Branches for early isolates are indicated in blue, late isolates in red and PAO1 in black.

Gray values within the branches represent the % of bootstrap values for 10,000 replicates. c) HCA of the 235 differentially expressed proteins when comparing late *vs* early strains within the COG categories related to metabolism. Proteomes are represented by dashed lines for "cluster A" and continuous lines for "cluster B". Gray values within the branches represent the % of bootstrap values for 10,000 replicates. d) Parallel plots of the number of differentially expressed (DE) proteins within the COG categories related to metabolism in cluster A (Blue, shaded) and B (red, transparent). e) Metabolic maps showing the differences between early clinical strains *vs* PAO1 (left) and late *vs* early clinical strains (right) in pathways related to the catabolism of nutrients present in SCFM2 through central carbon metabolism. Arrows represent individual metabolite-conversions coloured by their pathway. Reactions are coloured if the underlining enzyme is differentially expressed in more than one clone type – either with dashed (downregulated) or full (upregulated) lines, or both. Enzymes responsible for each reaction are indicated by numbered circles. For details on individual enzymes, see Figure S2. Transporters are shown at the bottom as arrows crossing bacterial cell membrane with their specific transported metabolites. Asp, Glu and acetate are labelled with * to indicate that they are represented in two places on the map, due to their involvement in different parts of central carbon metabolism.

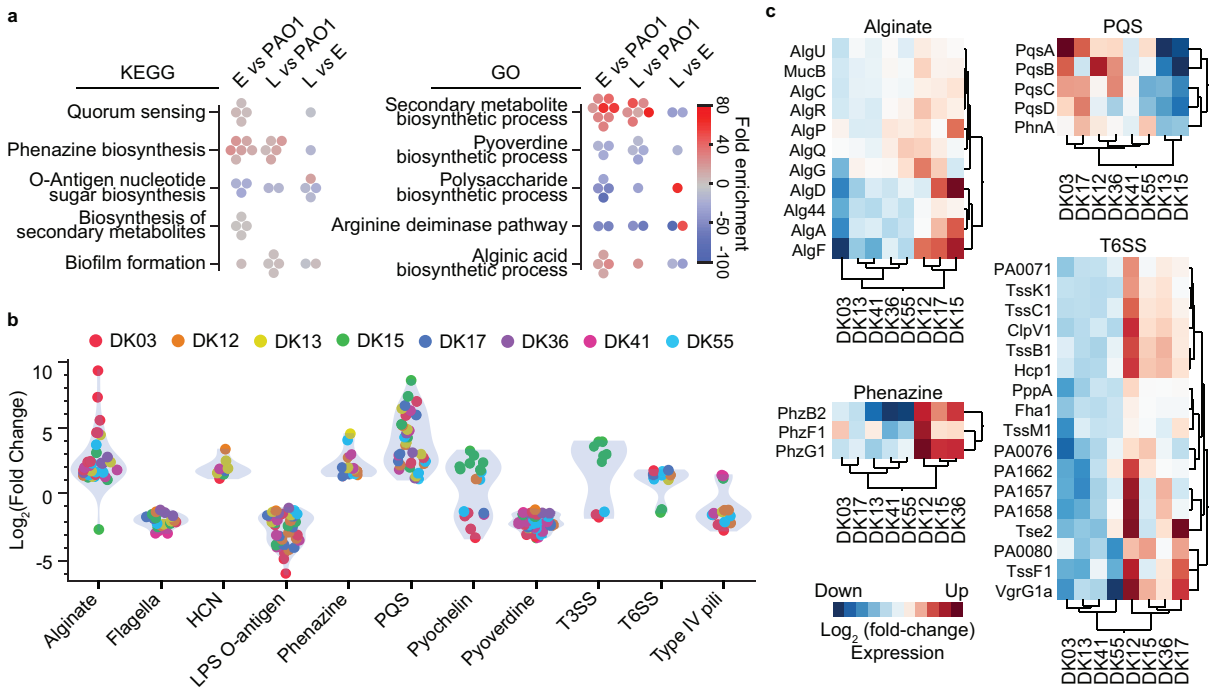

790 Figure 4: Expression of virulence factors differs in clinical strains *vs* PAO1. a) Enrichment
791 analysis for KEGG and GO terms by the specific comparisons (Early *vs* PAO1; Late *vs* PAO1;
792 Late *vs* Early). Icons represent individual lineages and are coloured by fold-enrichment. b)
793 Differential expression of virulence factors in early clinical strains *vs* PAO1. Only differentially
794 expressed proteins are represented and are coloured by clone type. c) HCA of differentially
795 expressed proteins of virulence factors in late *vs* early clinical strains.

796

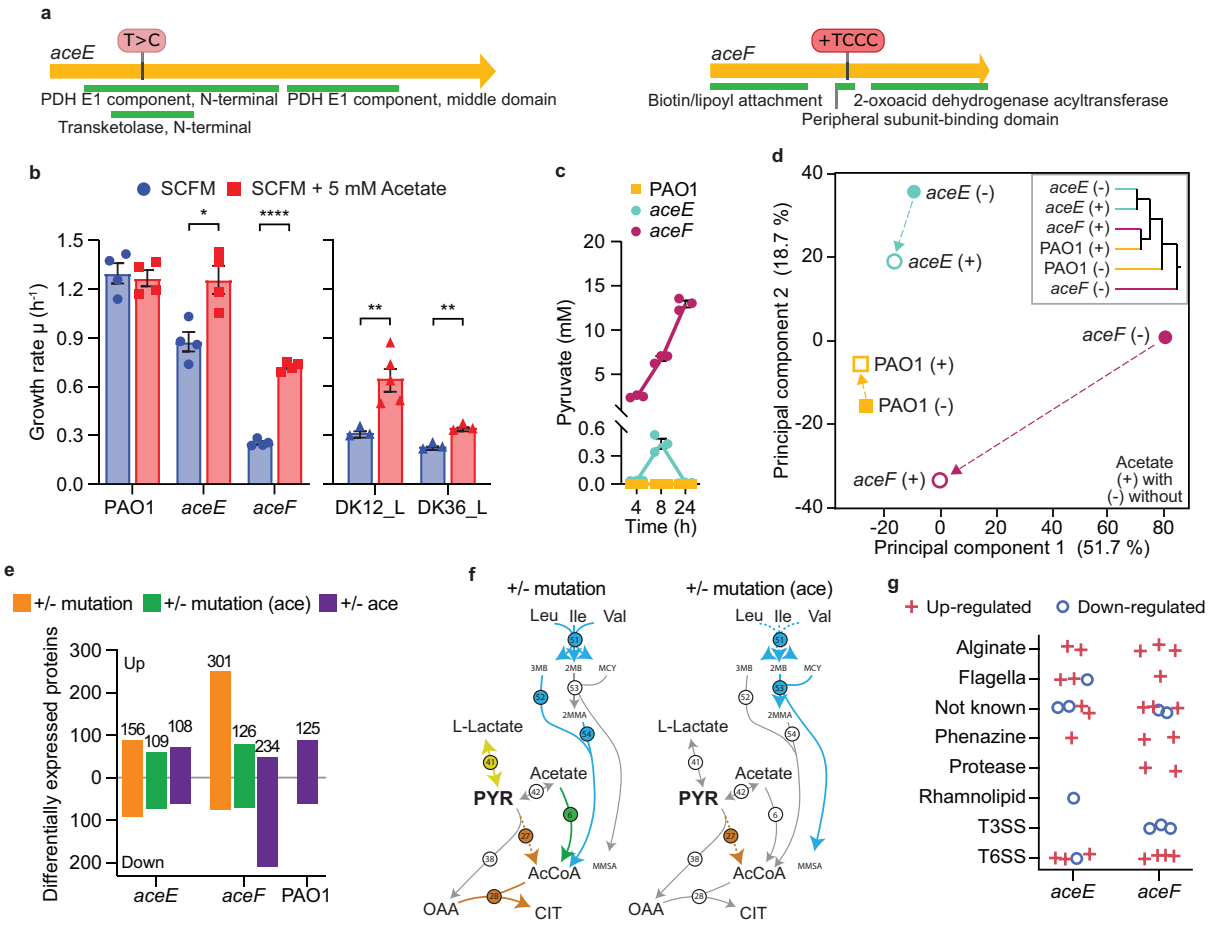

797

798 Figure 5: *aceE* and *aceF* mutations cause metabolic specialization. a) Schematic of the *aceE*
799 and *aceF* genes including location and type of mutation found in the DK36 (*aceE*) and DK12
800 (*aceF*) late strains. b) Growth rate (hour^{-1}) in SCFM2 (blue) and SCFM2 supplemented with 5
801 mM acetate (red) for PAO1, *aceE* and *aceF* mutant strains, and DK12 and DK36 late clinical
802 isolates. Bars indicate mean ± SEM, with icons representing biological replicates. Statistical
803 significance is assessed by two-tailed unpaired parametric Welch t-test and indicated as * (p
804 < 0.05), ** ($p < 0.01$) or **** ($p < 0.0001$). c) Pyruvate secretion (mM) for PAO1 wt (yellow),

805 *aceE* (cyan) and *aceF* (magenta) mutant strains over 24 hours. Icons represent biological
806 replicates. d) PCA and HCA of whole-cell proteomics for PAO1 wt and *aceE* and *aceF* mutant
807 strains. Filled icons indicate without (-) and unfilled icons indicate with (+) 5 mM acetate. e)
808 Number of differentially expressed proteins for mutant strain *vs* PAO1 wt comparisons: in
809 orange in absence of acetate (+/- mutation) and in green in presence of acetate (+/- mutation
810 (ace)). In purple the number of differentially expressed proteins for either the PAO1 wt or the
811 *aceE* or *aceF* mutant strain in presence *vs* absence of acetate (+/- acetate). f) Metabolic map
812 of enzymes related to pyruvate and acetyl-CoA metabolism for mutant strains *vs* PAO1 in
813 absence (left) or presence (right) of acetate. Reactions are coloured by their pathway if the
814 underlining enzyme is differentially expressed (dashed if downregulated or continuous if
815 upregulated). Enzymes responsible for each reaction are indicated by numbered circles. For
816 details on individual enzymes, see Figure S6. g) Differentially expressed proteins involved in
817 virulence in *aceE* and *aceF* mutant strains *vs* PAO1 in absence of acetate. Icons indicate
818 specific proteins that are upregulated (red plus) or downregulated (blue circle).

819

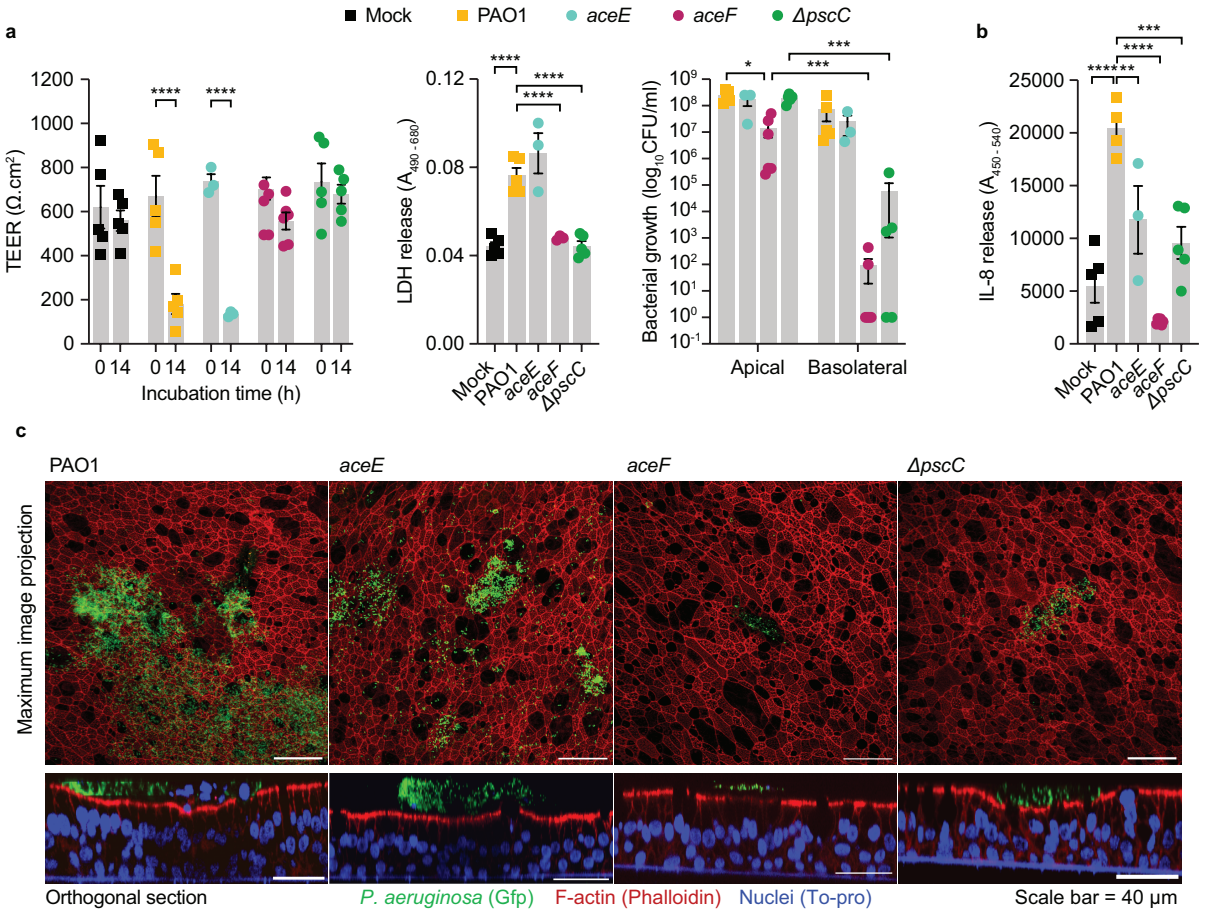

820

821 Figure 6**:** Aggressiveness of *aceE* and *aceF* strains in Air-Liquid Interface airway infections. a)
822 Mean ± SEM of Transepithelial Electrical Resistance (TEER) ($\Omega \cdot cm^2$), LDH release and Colony
823 Forming Units (CFU) in the apical and basolateral ALI compartments after 14 hours of infection
824 in fully differentiated BCi-NS1.1 cells. b) IL-8 release into the basolateral media indicating
825 immunogenicity caused by the invading bacteria. Icons represent each biological replicates.
826 Mock represents un-infected control cells. Statistical significance was determined by Two-
827 Way ANOVA for TEER and CFU measurements and One-Way ANOVA for LDH and IL-8
828 measurements and indicated as * ($p < 0.05$), ** ($p < 0.01$), *** ($p < 0.001$) and **** ($p <$
829 0.0001). c) Confocal images of ALI transwells following infection with *P. aeruginosa* in green
830 (GFP), epithelium in red (Phalloidin) and nuclei in blue (To-pro). Scale bar = 40 μm.

831

832 Figure S1: a) Number of differentially expressed proteins (top) and Log_2(Fold change) of
833 individual differentially expressed proteins in late vs. early clinical isolates, separated by
834 lineage and on the x-axis by COG categories. b) Complete enrichment analysis showing fold-
835 enrichments separated by comparison and lineage on x-axis and by KEGG and GO terms on y-
836 axis.

837

838 Figure S2: a) Metabolic map in the same style as Fig. 3E for late clinical strains vs PAO1. b)
839 Table of genes/Locus Tags of all metabolic enzymes included in the map. c-d) Bar charts
840 showing Log_2(Fold change) of all differentially expressed proteins highlighted on the
841 metabolic maps. Icons coloured by lineage and separated into three comparisons on x-axis
842 (Early vs PAO1; Late vs Early; Late vs PAO1). Panel c contains metabolic enzymes and panel d
843 contains transporters.

844

845 Figure S3: a) Hierarchical cluster analysis in the same style as Fig. 4C, showing differential
846 expression in late vs early clinical strains for several more virulence categories. b) The
847 Log_2(Fold change) of differentially expressed proteins in late vs early clinical strains separated
848 into the relevant virulence categories and further separated into the two main clusters from

849 panel a. Icons are coloured by lineage and lines depict the difference in mean Log_2(Fold
850 change) between the two clusters.

851

852 Figure S4: Schematic of all 18 unique mutations observed for *aceE* (top) and *aceF* (bottom) in
853 our collection of clinical isolates of *P. aeruginosa*. Grey lines indicate mutation site and letters
854 indicate nucleotide-sequence coloured by type of mutation.

855

856 Figure S5: a) Potential for biofilm formation (surface attachment) of PAO1 wt (blue), as well
857 as *aceE* (red) and *aceF* (green) mutant strains and DK12 & DK36 late clinical strains after 24
858 and 48 hours respectively. For the clinical isolates, strain is indicated on the x-axes and
859 incubation time is indicated as blue (24 hours) and red (48 hours). Attachment is measured
860 as the ratio of surface-attached cells (OD_{590}) to total number of cells (OD_{600}) after incubation.
861 For PAO1 wt and *aceE* and *aceF* mutants, all strains were compared by One-Way ANOVA. For
862 clinical isolates, each strain was compared to itself after 24 and 48 hours of incubation
863 respectively, using two-tailed unpaired parametric Welch t-test. Significance is indicated as
864 'ns' ($p > 0.05$), * ($p < 0.05$), ** ($p < 0.01$), *** ($p < 0.001$). Same colouring and statistical analysis
865 for PAO1 and mutant strains in panel b-d. b) Motility measured as the diameter (mm) of the
866 zone of growth in motility plates (LB agar). Swimming motility was clearly visible after 24
867 hours of incubation. Swarming and twitching plates required 48 hours of incubation. c) Redox
868 sensitivity measured as the diameter of the clearance zone (mm) on bacterial lawns (LB agar)
869 of each strain from H_2O_2 diffusion disks after 24 hours. d) Pyoverdine production measured
870 as relative fluorescence (F/OD_{600}) of each strain after 24 hours of growth in King's B medium.
871 For panel a-d, icons indicate biological replicates and bars represent the mean ± SEM. e) MICs
872 of PAO1 wt and *aceE* and *aceF* mutant strains. Each cell represents the maxOD of growth
873 curves under the given condition, following the colour gradient to the right of each heatmap.
874 The MIC is the concentration where no growth is observed (white). Each heat map shows the
875 MIC for all three strains for a given antibiotic (Ceftazidime, Meropenem, Piperacillin,
876 Azithromycin, Chloramphenicol, Ciprofloxacin and Tobramycin). Concentrations (μg/mL)
877 increase 2-fold downward on the vertical axis and the specific strain is given on the horizontal

878 axis. Azithromycin MICs were determined in LB, while all other MICs were determined in
879 SCFM2. Piperacillin was used in combination with the β-lactamase inhibitor Tazobactam.

880

881 Figure S6: a) Metabolic map in the same style as Fig. 3E for *aceF* mutant strain vs PAO1
882 reference in SCFM2 in absence (left) and presence (right) of acetate. b) Parallel plot showing
883 the number of differentially expressed proteins, separated by metabolic COG categories, in
884 *aceE* (cyan) and *aceF* (magenta) mutant strains vs PAO1. c) Enrichment analysis showing fold
885 enrichment on x-axis separated by KEGG and GO terms on y-axis for *aceE* (left) and *aceF* (right)
886 mutant strains vs PAO1. d) The -Log2(Fold change) of the Dnr transcriptional regulator in late
887 vs early clinical isolates (Same holds for late strains vs PAO1) for lineages in Cluster A (left)
888 and B (middle), as well as in the *aceE* mutant strain (right) when compared to PAO1 wt in
889 SCFM2 in absence (+/- mutation) and presence (Ace) of acetate or when compared to itself in
890 presence of acetate (+/- Acetate).

891

892 Figure S7: Longitudinal collection of *P. aeruginosa* clinical isolates from CF airways. Icons
893 indicate isolates carrying mutations in genes encoding PDHc (red squares) and/or T3SS
894 (purple triangles) proteins, as well as isolates with no mutations in either (grey dots). Isolates
895 are separated by Clone Type and further separated by patient-specific lineages within Clone
896 Types (A, B, C). The x-axis shows the length of infection (years) since the first isolate of the
897 given lineage.

898 References

899 1. Murray, C.J., Ikuta, K.S., Sharara, F., Swetschinski, L., Robles Aguilar, G., Gray, A., Han, C.,
900 Bisignano, C., Rao, P., Wool, E., et al. (2022). Global burden of bacterial antimicrobial
901 resistance in 2019: a systematic analysis. The Lancet *6736*. 10.1016/S0140-6736(21)02724-0.

902 2. La Rosa, R., Johansen, H.K., and Molin, S. (2022). Persistent Bacterial Infections, Antibiotic
903 Treatment Failure, and Microbial Adaptive Evolution. Antibiotics *11*, 419.
904 10.3390/antibiotics11030419.

905 3. Haney, E.F., and Hancock, R.E.W. (2022). Addressing Antibiotic Failure—Beyond Genetically
906 Encoded Antimicrobial Resistance. Frontiers in Drug Discovery *2*, 1–7.
907 10.3389/fddsv.2022.892975.

908 4. Rossi, E., La Rosa, R., Bartell, J.A., Marvig, R.L., Haagensen, J.A.J., Sommer, L.M., Molin, S., and
909 Johansen, H.K. (2021). Pseudomonas aeruginosa adaptation and evolution in patients with
910 cystic fibrosis. Nat Rev Microbiol *19*, 331–342. 10.1038/s41579-020-00477-5.

911 5. Armbruster, C.R., Marshall, C.W., Garber, A.I., Melvin, J.A., Zemke, A.C., Moore, J., Zamora,
912 P.F., Li, K., Fritz, I.L., Manko, C.D., et al. (2021). Adaptation and genomic erosion in
913 fragmented Pseudomonas aeruginosa populations in the sinuses of people with cystic
914 fibrosis. Cell Rep *37*. 10.1016/j.celrep.2021.109829.

915 6. Cramer, N., Klockgether, J., and Tümmler, B. (2023). Microevolution of Pseudomonas
916 aeruginosa in the airways of people with cystic fibrosis. Curr Opin Immunol *83*, 102328.
917 10.1016/j.coi.2023.102328.

918 7. Camus, L., Vandenesch, F., and Moreau, K. (2021). From genotype to phenotype: Adaptations
919 of Pseudomonas aeruginosa to the cystic fibrosis environment. Microb Genom *7*.
920 10.1099/mgen.0.000513.

921 8. Bartell, J.A., Sommer, L.M., Haagensen, J.A.J., Loch, A., Espinosa, R., Molin, S., and Johansen,
922 H.K. (2019). Evolutionary highways to persistent bacterial infection. Nat Commun *10*, 629.
923 10.1038/s41467-019-08504-7.

924 9. La Rosa, R., Johansen, H.K., and Molin, S. (2019). Adapting to the Airways: Metabolic
925 Requirements of Pseudomonas aeruginosa during the Infection of Cystic Fibrosis Patients.
926 Metabolites *9*, 234. 10.3390/metabo9100234.

927 10. Brown, S.A., Palmer, K.L., and Whiteley, M. (2008). Revisiting the host as a growth medium.
928 Nat Rev Microbiol *6*, 657–666. 10.1038/nrmicro1955.

929 11. Diaz, M.R., King, J.M., and Yahr, T.L. (2011). Intrinsic and extrinsic regulation of type III
930 secretion gene expression in Pseudomonas aeruginosa. Front Microbiol *2*, 1–10.
931 10.3389/fmicb.2011.00089.

932 12. Li, L., Meng, H., Gu, D., Li, Y., and Jia, M. (2019). Molecular mechanisms of Vibrio
933 parahaemolyticus pathogenesis. Microbiol Res *222*, 43–51. 10.1016/j.micres.2019.03.003.

934 13. Malik-Kale, P., Jolly, C.E., Lathrop, S., Winfree, S., Luterbach, C., and Steele-Mortimer, O.
935 (2011). Salmonella- at home in the host cell. Front Microbiol *2*, 1–9.
936 10.3389/fmicb.2011.00125.

937 14. Flannagan, R.S., Cosío, G., and Grinstein, S. (2009). Antimicrobial mechanisms of phagocytes
938 and bacterial evasion strategies. Nat Rev Microbiol *7*, 355–366. 10.1038/nrmicro2128.

939 15. Horna, G., and Ruiz, J. (2021). Type 3 secretion system of Pseudomonas aeruginosa. Microbiol
940 Res *246*, 126719. 10.1016/j.micres.2021.126719.

941 16. Hauser, A.R. (2009). The type III secretion system of Pseudomonas aeruginosa: Infection by
942 injection. Nat Rev Microbiol *7*, 654–665. 10.1038/nrmicro2199.

943 17. Malhotra, S., Hayes, D., and Wozniak, D.J. (2019). Mucoid Pseudomonas aeruginosa and
944 regional inflammation in the cystic fibrosis lung. Journal of Cystic Fibrosis *18*, 796–803.
945 10.1016/j.jcf.2019.04.009.

946 18. Govan, J.R., and Deretic, V. (1996). Microbial pathogenesis in cystic fibrosis: mucoid
947 Pseudomonas aeruginosa and Burkholderia cepacia. Microbiol Rev *60*, 539–574.
948 10.1111/j.1365-2672.2007.03706.x.

949 19. Henry, R.L., Mellis, C.M., and Petrovic, L. (1992). Mucoid Pseudomonas aeruginosa is a
950 marker of poor survival in cystic fibrosis. Pediatr Pulmonol *12*, 158–161.
951 10.1002/ppul.1950120306.

952 20. Heim, C.E., Bosch, M.E., Yamada, K.J., Aldrich, A.L., Chaudhari, S.S., Klinkebiel, D., Gries, C.M.,
953 Alqarzaee, A.A., Li, Y., Thomas, V.C., et al. (2020). Lactate production by Staphylococcus
954 aureus biofilm inhibits HDAC11 to reprogramme the host immune response during persistent
955 infection. Nat Microbiol *5*, 1271–1284. 10.1038/s41564-020-0756-3.

956 21. Tomlinson, K.L., Lung, T.W.F., Dach, F., Annavajhala, M.K., Gabryszewski, S.J., Groves, R.A.,
957 Drikic, M., Francoeur, N.J., Sridhar, S.H., Smith, M.L., et al. (2021). Staphylococcus aureus
958 induces an itaconate-dominated immunometabolic response that drives biofilm formation.
959 Nat Commun *12*, 1–13. 10.1038/s41467-021-21718-y.

960 22. Riquelme, S.A., Liimatta, K., Wong Fok Lung, T., Fields, B., Ahn, D., Chen, D., Lozano, C., Sáenz,
961 Y., Uhlemann, A.C., Kahl, B.C., et al. (2020). Pseudomonas aeruginosa Utilizes Host-Derived
962 Itaconate to Redirect Its Metabolism to Promote Biofilm Formation. Cell Metab *31*, 1091-
963 1106.e6. 10.1016/j.cmet.2020.04.017.

964 23. La Rosa, R., Johansen, H.K., and Molin, S. (2018). Convergent Metabolic Specialization
965 through Distinct Evolutionary Paths in Pseudomonas aeruginosa. mBio *9*, e00269-18.
966 10.1128/mBio.00269-18.

967 24. Behrends, V., Bell, T.J., Liebeke, M., Cordes-Blauert, A., Ashraf, S.N., Nair, C., Zlosnik, J.E.A.,
968 Williams, H.D., and Bundy, J.G. (2013). Metabolite Profiling to Characterize Disease-related
969 Bacteria. Journal of Biological Chemistry *288*, 15098–15109. 10.1074/jbc.M112.442814.

970 25. La Rosa, R., Rossi, E., Feist, A.M., Johansen, H.K., and Molin, S. (2021). Compensatory
971 evolution of Pseudomonas aeruginosa's slow growth phenotype suggests mechanisms of
972 adaptation in cystic fibrosis. Nat Commun *12*, 3186. 10.1038/s41467-021-23451-y.

973 26. Lopatkin, A.J., Bening, S.C., Manson, A.L., Stokes, J.M., Kohanski, M.A., Badran, A.H., Earl,
974 A.M., Cheney, N.J., Yang, J.H., and Collins, J.J. (2021). Clinically relevant mutations in core
975 metabolic genes confer antibiotic resistance. Science (1979) *371*, eaba0862.
976 10.1126/science.aba0862.

977 27. Martínez, J.L., and Rojo, F. (2011). Metabolic regulation of antibiotic resistance. FEMS
978 Microbiol Rev *35*, 768–789. 10.1111/j.1574-6976.2011.00282.x.

979 28. Chung, J.C.S., Rzhepishevska, O., Ramstedt, M., and Welch, M. (2013). Type III secretion
980 system expression in oxygen-limited Pseudomonas aeruginosa cultures is stimulated by
981 isocitrate lyase activity. Open Biol *3*. 10.1098/rsob.120131.

982 29. Linares, J.F., López, J.A., Camafeita, E., Albar, J.P., Rojo, F., and Martínez, J.L. (2005).
983 Overexpression of the multidrug efflux pumps MexCD-OprJ and MexEF-OprN is associated
984 with a reduction of type III secretion in Pseudomonas aeruginosa. J Bacteriol *187*, 1384–1391.
985 10.1128/JB.187.4.1384-1391.2005.

986 30. Dacheux, D., Epaulard, O., De Groot, A., Guery, B., Leberre, R., Attree, I., Polack, B., and
987 Toussaint, B. (2002). Activation of the Pseudomonas aeruginosa type III secretion system
988 requires an intact pyruvate dehydrogenase aceAB operon. Infect Immun *70*, 3973–3977.
989 10.1128/IAI.70.7.3973-3977.2002.

990 31. Olivares, J., Álvarez-Ortega, C., and Martinez, J.L. (2014). Metabolic Compensation of Fitness
991 Costs Associated with Overexpression of the Multidrug Efflux Pump MexEF-OprN in
992 Pseudomonas aeruginosa. Antimicrob Agents Chemother *58*, 3904–3913.
993 10.1128/aac.00121-14.

994 32. Drevinek, P., Canton, R., Johansen, H.K., Hoffman, L., Coenye, T., Burgel, P., and Davies, J.C.
995 (2022). New concepts in antimicrobial resistance in cystic fibrosis respiratory infections.
996 Journal of Cystic Fibrosis *21*, 937–945. 10.1016/j.jcf.2022.10.005.

997 33. Kao, K.K., and Fink, M.P. (2010). The biochemical basis for the anti-inflammatory and
998 cytoprotective actions of ethyl pyruvate and related compounds. Biochem Pharmacol *80*,
999 151–159. 10.1016/j.bcp.2010.03.007.

1000 34. O'Donnell-Tormey, J., Nathan, C.F., Lanks, K., DeBoer, C.J., and de la Harpe, J. (1987).
1001 Secretion of pyruvate. An antioxidant defense of mammalian cells. Journal of Experimental
1002 Medicine *165*, 500–514. 10.1084/jem.165.2.500.

1003 35. Li, J., Diao, B., Guo, S., Huang, X., Yang, C., Feng, Z., Yan, W., Ning, Q., Zheng, L., Chen, Y., et al.
1004 (2017). VSIG4 inhibits proinflammatory macrophage activation by reprogramming
1005 mitochondrial pyruvate metabolism. Nat Commun *8*, 1–13. 10.1038/s41467-017-01327-4.

1006 36. Marvig, R.L., Sommer, L.M., Molin, S., and Johansen, H.K. (2015). Convergent evolution and
1007 adaptation of Pseudomonas aeruginosa within patients with cystic fibrosis. Nat Genet *47*, 57–
1008 64. 10.1038/ng.3148.

1009 37. Palmer, K.L., Aye, L.M., and Whiteley, M. (2007). Nutritional Cues Control Pseudomonas
1010 aeruginosa Multicellular Behavior in Cystic Fibrosis Sputum. J Bacteriol *189*, 8079–8087.
1011 10.1128/JB.01138-07.

1012 38. Thomas, S.R. (2000). Increased sputum amino acid concentrations and auxotrophy of
1013 Pseudomonas aeruginosa in severe cystic fibrosis lung disease. Thorax *55*, 795–797.
1014 10.1136/thorax.55.9.795.

1015 39. Price-Whelan, A., Dietrich, L.E.P., and Newman, D.K. (2007). Pyocyanin Alters Redox
1016 Homeostasis and Carbon Flux through Central Metabolic Pathways in Pseudomonas
1017 aeruginosa PA14. J Bacteriol *189*, 6372–6381. 10.1128/JB.00505-07.

1018 40. Schiessl, K.T., Hu, F., Jo, J., Nazia, S.Z., Wang, B., Price-Whelan, A., Min, W., and Dietrich, L.E.P.
1019 (2019). Phenazine production promotes antibiotic tolerance and metabolic heterogeneity in
1020 Pseudomonas aeruginosa biofilms. Nat Commun *10*, 1–10. 10.1038/s41467-019-08733-w.

1021 41. Qin, S., Xiao, W., Zhou, C., Pu, Q., Deng, X., Lan, L., Liang, H., Song, X., and Wu, M. (2022).
1022 Pseudomonas aeruginosa: pathogenesis, virulence factors, antibiotic resistance, interaction
1023 with host, technology advances and emerging therapeutics. Signal Transduct Target Ther *7*,
1024 199. 10.1038/s41392-022-01056-1.

1025 42. Moradali, M.F., Ghods, S., and Rehm, B.H.A. (2017). Pseudomonas aeruginosa Lifestyle: A
1026 Paradigm for Adaptation, Survival, and Persistence. Front Cell Infect Microbiol *7*, 39.
1027 10.3389/fcimb.2017.00039.

1028 43. Rossi, E., Falcone, M., Molin, S., and Johansen, H.K. (2018). High-resolution in situ
1029 transcriptomics of Pseudomonas aeruginosa unveils genotype independent patho-
1030 phenotypes in cystic fibrosis lungs. Nat Commun *9*, 3459. 10.1038/s41467-018-05944-5.

1031 44. Eschbach, M., Schreiber, K., Trunk, K., Buer, J., Jahn, D., and Schobert, M. (2004). Long-term
1032 anaerobic survival of the opportunistic pathogen Pseudomonas aeruginosa via pyruvate
1033 fermentation. J Bacteriol *186*, 4596–4604. 10.1128/JB.186.14.4596-4604.2004.

1034 45. Dang, J., Wang, T., Wen, J., and Liang, H. (2022). An Important Role of the Type VI Secretion
1035 System of Pseudomonas aeruginosa Regulated by Dnr in Response to Anaerobic
1036 Environments. Microbiol Spectr *10*. 10.1128/spectrum.01533-22.

1037 46. Krieger, R., Rompf, A., Schobert, M., and Jahn, D. (2002). The Pseudomonas aeruginosa hemA
1038 promoter is regulated by Anr, Dnr, NarL and Integration Host Factor. Molecular Genetics and
1039 Genomics *267*, 409–417. 10.1007/s00438-002-0672-7.

1040 47. Yang, R., Zhu, S., and Tonnessen, T.I. (2016). Ethyl pyruvate is a novel anti-inflammatory agent
1041 to treat multiple inflammatory organ injuries. Journal of Inflammation (United Kingdom) *13*,
1042 1–11. 10.1186/s12950-016-0144-1.

1043 48. Barth, A.L., and Pitt, T.L. (1996). The high amino-acid content of sputum from cystic fibrosis
1044 patients promotes growth of auxotrophic Pseudomonas aeruginosa. J Med Microbiol *45*,
1045 110–119. 10.1099/00222615-45-2-110.

1046 49. Winstanley, C., O'Brien, S., and Brockhurst, M.A. (2016). Pseudomonas aeruginosa
1047 Evolutionary Adaptation and Diversification in Cystic Fibrosis Chronic Lung Infections. Trends
1048 Microbiol *24*, 327–337. 10.1016/j.tim.2016.01.008.

1049 50. Li, H., Xia, Y., Tian, Z., Jin, Y., Bai, F., Cheng, Z., Swietnicki, W., Wu, W., and Pan, X. (2022).
1050 Dihydrolipoamide Acetyltransferase AceF Influences the Type III Secretion System and
1051 Resistance to Oxidative Stresses through RsmY/Z in Pseudomonas aeruginosa.
1052 Microorganisms *10*. 10.3390/MICROORGANISMS10030666.

1053 51. Galli, F., Battistoni, A., Gambari, R., Pompella, A., Bragonzi, A., Pilolli, F., Iuliano, L., Piroddi,
1054 M., Dechecchi, M.C., and Cabrini, G. (2012). Oxidative stress and antioxidant therapy in cystic
1055 fibrosis. Biochim Biophys Acta Mol Basis Dis *1822*, 690–713. 10.1016/j.bbadis.2011.12.012.

1056 52. Relja, B., Omid, N., Schaible, A., Perl, M., Meier, S., Oppermann, E., Lehnert, M., and Marzi, I.
1057 (2015). Pre- or post-treatment with ethanol and ethyl pyruvate results in distinct anti-

1058 inflammatory responses of human lung epithelial cells triggered by interleukin-6. Mol Med
1059 Rep *12*, 2991–2998. 10.3892/mmr.2015.3764.

1060 53. Hollenbach, M., Hintersdorf, A., Huse, K., Sack, U., Bigl, M., Groth, M., Santel, T., Buchold, M.,
1061 Lindner, I., Otto, A., et al. (2008). Ethyl pyruvate and ethyl lactate down-regulate the
1062 production of pro-inflammatory cytokines and modulate expression of immune receptors.
1063 Biochem Pharmacol *76*, 631–644. 10.1016/j.bcp.2008.06.006.

1064 54. Chakhtoura, M., Chain, R.W., Sato, P.Y., Qiu, C.C., Lee, M.H., Meissler, J.J., Eisenstein, T.K.,
1065 Koch, W.J., Caricchio, R., and Gallucci, S. (2019). Ethyl pyruvate modulates murine dendritic
1066 cell activation and survival through their immunometabolism. Front Immunol *10*, 1–16.
1067 10.3389/fimmu.2019.00030.

1068 55. Kimura, A., Yamauchi, Y., Hodono, S., Stewart, N.J., Hosokawa, O., Hagiwara, Y., Imai, H., and
1069 Fujiwara, H. (2017). Treatment response of ethyl pyruvate in a mouse model of chronic
1070 obstructive pulmonary disease studied by hyperpolarized 129Xe MRI. Magn Reson Med *78*,
1071 721–729. 10.1002/mrm.26458.

1072 56. Min, B.K., Park, S., Kang, H.J., Kim, D.W., Ham, H.J., Ha, C.M., Choi, B.J., Lee, J.Y., Oh, C.J., Yoo,
1073 E.K., et al. (2019). Pyruvate dehydrogenase kinase is a metabolic checkpoint for polarization
1074 of macrophages to the M1 phenotype. Front Immunol *10*. 10.3389/fimmu.2019.00944.

1075 57. Zhang, W., Zhang, S.L., Hu, X., and Tam, K.Y. (2015). Targeting Tumor Metabolism for Cancer
1076 Treatment: Is Pyruvate Dehydrogenase Kinases (PDKs) a Viable Anticancer Target? Int J Biol
1077 Sci *11*, 1390. 10.7150/IJBS.13325.

1078 58. McCall, C.E., Zabalawi, M., Liu, T., Martin, A., Long, D.L., Buechler, N.L., Arts, R.J.W., Netea,
1079 M., Yoza, B.K., Stacpoole, P.W., et al. (2018). Pyruvate dehydrogenase complex stimulation
1080 promotes immunometabolic homeostasis and sepsis survival. JCI Insight *3*.
1081 10.1172/jci.insight.99292.

1082 59. Meiser, J., Krämer, L., Sapcariu, S.C., Battello, N., Ghelfi, J., D'Herouel, A.F., Skupin, A., and
1083 Hiller, K. (2016). Pro-inflammatory macrophages sustain pyruvate oxidation through pyruvate
1084 dehydrogenase for the synthesis of itaconate and to enable cytokine expression. Journal of
1085 Biological Chemistry *291*, 3932–3946. 10.1074/jbc.M115.676817.

1086 60. O'Neill, L.A.J., and Artyomov, M.N. (2019). Itaconate: the poster child of metabolic
1087 reprogramming in macrophage function. Nat Rev Immunol *19*, 273–281. 10.1038/S41577-
1088 019-0128-5.

1089 61. Domínguez-Andrés, J., Novakovic, B., Li, Y., Scicluna, B.P., Gresnigt, M.S., Arts, R.J.W., Oosting,
1090 M., Moorlag, S.J.C.F.M., Groh, L.A., Zwaag, J., et al. (2019). The Itaconate Pathway Is a Central
1091 Regulatory Node Linking Innate Immune Tolerance and Trained Immunity. Cell Metab *29*,
1092 211-220.e5. 10.1016/J.CMET.2018.09.003.

1093 62. Bailey, J.D., Diotallevi, M., Nicol, T., McNeill, E., Shaw, A., Chuaiphichai, S., Hale, A., Starr, A.,
1094 Nandi, M., Stylianou, E., et al. (2019). Nitric Oxide Modulates Metabolic Remodeling in
1095 Inflammatory Macrophages through TCA Cycle Regulation and Itaconate Accumulation. Cell
1096 Rep *28*, 218-230.e7. 10.1016/j.celrep.2019.06.018.

1097 63. Zhu, X., Long, D., Zabalawi, M., Ingram, B., Yoza, B.K., Stacpoole, P.W., and McCall, C.E.
1098 (2020). Stimulating pyruvate dehydrogenase complex reduces itaconate levels and enhances

1099 TCA cycle anabolic bioenergetics in acutely inflamed monocytes. J Leukoc Biol *107*, 467–484.
1100 10.1002/JLB.3A1119-236R.

1101 64. Riquelme, S.A., and Prince, A. (2020). Airway immunometabolites fuel Pseudomonas
1102 aeruginosa infection. Respir Res *21*, 1–10. 10.1186/s12931-020-01591-x.

1103 65. Baldassi, D., Gabold, B., and Merkel, O.M. (2021). Air−Liquid Interface Cultures of the Healthy
1104 and Diseased Human Respiratory Tract: Promises, Challenges, and Future Directions. Adv
1105 Nanobiomed Res *1*, 2000111. 10.1002/anbr.202000111.

1106 66. Cavaleiro, A.M., Kim, S.H., Seppälä, S., Nielsen, M.T., and Nørholm, M.H.H. (2015). Accurate
1107 DNA assembly and genome engineering with optimized uracil excision cloning. ACS Synth Biol
1108 *4*, 1042–1046. 10.1021/acssynbio.5b00113.

1109 67. Chen, W., Zhang, Y., Zhang, Y., Pi, Y., Gu, T., Song, L., Wang, Y., and Ji, Q. (2018). CRISPR/Cas9-
1110 based genome editing in Pseudomonas aeruginosa and cytidine deaminase-mediated base
1111 editing in Pseudomonas species. iScience *6*, 222–231. 10.1016/j.isci.2018.07.024.

1112 68. Choi, K.H., and Schweizer, H.P. (2006). mini-Tn7 insertion in bacteria with single attTn7 sites:
1113 example Pseudomonas aeruginosa. Nat Protoc *1*, 153–161. 10.1038/NPROT.2006.24.

1114 69. Turner, K.H., Wessel, A.K., Palmer, G.C., Murray, J.L., and Whiteley, M. (2015). Essential
1115 genome of Pseudomonas aeruginosa in cystic fibrosis sputum. Proc Natl Acad Sci U S A *112*,
1116 4110–4115. 10.1073/pnas.1419677112.

1117 70. Deschamps, E., Schaumann, A., Schmitz-Afonso, I., Afonso, C., Dé, E., Loutelier-Bourhis, C.,
1118 and Alexandre, S. (2021). Membrane phospholipid composition of Pseudomonas aeruginosa
1119 grown in a cystic fibrosis mucus-mimicking medium. Biochimica et Biophysica Acta (BBA) -
1120 Biomembranes *1863*, 183482. 10.1016/j.bbamem.2020.183482.

1121 71. Pedersen, B.H., Gurdo, N., Johansen, H.K., Molin, S., Nikel, P.I., and la Rosa, R. (2021). High-
1122 throughput dilution-based growth method enables time-resolved exo-metabolomics of
1123 Pseudomonas putida and Pseudomonas aeruginosa. Microb Biotechnol *0*, 1–13.
1124 10.1111/1751-7915.13905.

1125 72. Walters, M.S., Gomi, K., Ashbridge, B., Moore, M.A.S., Arbelaez, V., Heldrich, J., Ding, B.-S.,
1126 Rafii, S., Staudt, M.R., and Crystal, R.G. (2013). Generation of a human airway epithelium
1127 derived basal cell line with multipotent differentiation capacity. Respir Res *14*, 135.
1128 10.1186/1465-9921-14-135.

1129 73. Behrends, V., Williams, H.D., and Bundy, J.G. (2014). Metabolic Footprinting: Extracellular
1130 Metabolomic Analysis. In Pseudomonas Methods and Protocols, A. Filloux and J.-L. Ramos,
1131 eds. (Springer New York), pp. 281–292. 10.1007/978-1-4939-0473-0_23.

1132 74. Callister, S.J., Barry, R.C., Adkins, J.N., Johnson, E.T., Qian, W.J., Webb-Robertson, B.J.M.,
1133 Smith, R.D., and Lipton, M.S. (2006). Normalization approaches for removing systematic
1134 biases associated with mass spectrometry and label-free proteomics. J Proteome Res *5*, 277–
1135 286. 10.1021/PR050300L.

1136